

Towards an Ultra Sensitive Seismic Accelerometer

Pieter Kamp, *Student MSc. Electrical Engineering, Transducer Science & Technology, University of Twente*
MSc. Committee: Prof. dr. ir. J.C. Lötters, dr. ir. R.J. Wiegerink, dr. ir. A.J. Annema, dr. ir. R.A. Brookhuis

Abstract—A fourth generation MEMS-based silicon accelerometer is designed and fabricated in the process of developing an accelerometer to be used as an ultra sensitive seismometer for noise subtraction arrays. The device uses a novel ratchet system actuated by thermal actuators to compress precurved springs to increase the sensitivity of the system. The fabrication is based on a three-mask process, which is suitable for mass production. A first vertical application of such a device is designed and fabricated as a proof of concept. The flexures are rotated a predetermined angle so that, when placed vertically, the compressed system returns to its original position, effectively handling the offset of 1 g. A two-mask process is used for fabrication. A 2-fold stiffness reduction was obtained by compressing the pre-curved flexures 9 μm .

I. INTRODUCTION

THIS work's focus is twofold. On one hand it focuses on the modeling, design, fabrication and, mostly mechanical, characterization of an ultra sensitive micro-electro-mechanical system (MEMS) accelerometer. Secondly it focuses on the modeling, design, fabrication and characterization of a proof of concept vertical MEMS accelerometer. The work is carried out in collaboration with the Dutch subatomic particle physics institute Nikhef under the Senseis project [1].

A. Project Description

The goal of Senseis is the development of sensor technology for seismic monitoring to be used in Advanced VIRGO. VIRGO is a setup located in Cascina, near Pisa in Italy with the function of measuring gravitational waves. Gravitational waves are ripples in space-time fabric caused by fluctuations in gravity in for example rotating binary black hole systems. VIRGO is a very large Michelson interferometer with optical arms spanning 3 km. One of the main challenges is the attenuation of seismic activity affecting the positioning of the test masses and mirrors in the VIRGO setup. The sources of seismic activity are for example: tectonic activity, wind, tides and vehicles. One of the measures to reduce external noise is the placement of the entire setup under ultra high vacuum. Furthermore the test masses and mirrors are placed in an advanced suspension system of inverted pendulums and geometric antisprings effectively reducing the attenuation by external seismic activity by a factor of $\approx 10^{12}$ [2]. One effect of seismic noise known as Newtonian noise is unaffected by the advanced suspension system used. The seismic motion does not only impose motion directly on the interferometer, but also slightly affects the distribution of mass around the system. This effectively causes a fluctuation of the gravity around the mirrors, which cannot be shielded. One way of dealing with Newtonian noise is measuring it using a well placed array of a few thousand seismic sensors around the test masses and

then subtracting the noise field from the data measured by the interferometer [3]. This calls for very sensitive seismic sensors with a self-noise floor around $1 \text{ ng}/\sqrt{\text{Hz}}$, in which 1 ng is $9.81 \times 10^{-9} \text{ m/s}^2$. MEMS Sensors have a cost to scale advantage over conventional seismic instruments. Another possible application of such sensitive MEMS accelerometers is in the geophysical exploration industry, making it a commercially attractive development.

One of the main features of the accelerometer developed in collaboration with the Nikhef institute is the usage of geometric antisprings. Geometric antispring technology used in this work comprises of a set of precurved springs attached to the proofmass. The springs can be compressed using a set of thermal actuators and a ratchet system. The compression of the flexures effectively decreases the resonance frequency in the direction of interest of the mass-spring system. Decreasing the resonance frequency drastically increases the sensitivity of the system. The noise floor of a 4th generation MEMS accelerometer was found to be below $1 \text{ ng}/\sqrt{\text{Hz}}$ under appropriate vacuum conditions (self noise characterization not in this work).

One limitation of the 4th generation MEMS accelerometer is the relatively small full scale range, making it unsuitable for vertical applications. Measuring gravitational fluctuations in the vertical direction requires accelerometers to measure around a gravitational acceleration offset of 1 g. This means a sensor should either have a very large dynamic range or have some form of mechanical compensation. In this work the first steps in the development of a MEMS accelerometer which can be used in the vertical direction are made. The requirements for the accelerometers are shown in Table I.

TABLE I
ACCELEROMETER REQUIREMENTS

Specification	Value
Self-Noise Floor [$\text{ng}/\sqrt{\text{Hz}}$]	<1
Bandwidth [Hz]	1-100
Displacement Sensitivity [$\text{m}/\sqrt{\text{Hz}}$]	$<10 \times 10^{-12}$

B. State of Art Accelerometers

An overview of state of the art accelerometers from literature with their specifications is shown in Table II. Commercially available sensors exist, but are not very cost effective. MEMS Technology could be an economically attractive alternative, because of scaling advantages due to batch fabrication. Commercially available MEMS accelerometers from Sercel [4] and Colibrys [5] are based on capacitive readout and have noise floors of $20 \text{ ng}/\sqrt{\text{Hz}}$ above 1 Hz and $50 \text{ ng}/\sqrt{\text{Hz}}$ between

TABLE II
STATE OF THE ART ACCELEROMETER PERFORMANCE

Work	Mass [mg]	Resonant Frequency [Hz]	Dynamic Range [dB]	Self-Noise Floor [ng/ $\sqrt{\text{Hz}}$]	Sensitivity [V/g]	Max Signal [mg]	Transducer
Sercel DSU1-508 [4]	-	800	128	40 (10 - 200 Hz)	-	-	Capacitive
Colibrys [5]	-	1000	-	50	-	200	Capacitive
Kinemetrics Episensor 2 [6]	-	-	155	20	5	4000	Capacitive
Endevco Model 86 [7]	-	370	-	39 (@ 1 Hz)	10	500	Piezoelectric
Silicon Audio Ultra Low Noise [8]	-	300	183	8 (@ 1 Hz)	15	2000	Optical
Symphony Acoustics [9, p. 258]	-	-	160	1	-	-	Optical
PMD Scientific [10, p. 271]	-	140	150	0.5	-	-	Electrochemical
Krishnamoorthy et al. [11]	33.6	36	140	17	589	-	Optical
Fourquette et al. [12, p. 266]	10×10^3	-	-	10	-	-	Optical
Milligan et al. [13], [14]	-	-	120	9.8	26.2	80	Capacitive
Pike et al. [15], [16]	250	6-12	-	2	-	-	Capacitive

2 and 1000 Hz respectively. Another commercially available seismometer using a capacitive transducer is produced by Kinemetrics and has a self noise floor of 20 ng/ $\sqrt{\text{Hz}}$ together with a maximum signal of 4 g [6]. A piezoelectric accelerometer produced by Endevco has a noise floor of 39 ng/ $\sqrt{\text{Hz}}$ at 1 Hz [7]. Silicon Audio reengineered a geophone with an optical interferometer enabling a noise floor of 8 ng/ $\sqrt{\text{Hz}}$ [8]. Symphony Acoustics developed a laserinterferometer-based device having a self noise floor of 1 ng/ $\sqrt{\text{Hz}}$ in the range from 0.1 to 10 Hz [9, p. 258]. PMD Scientific [10, p. 271] uses an electrolyte solution as a liquid proof mass in a volume with partially elastic membranes. Within the volume are internal flow channels which house a series of cathodes and anodes for readout. Upon acceleration there exists a volume flow through the flow channels and the ion distribution of the electrolyte solution changes, ultimately leading to an output voltage. A theoretical noise floor of 0.5 ng/ $\sqrt{\text{Hz}}$ could be achieved. Several research groups worldwide are pushing the boundaries of noise floors in MEMS technology. Krishnamoorthy et al. [11] developed an accelerometer with an optomechanical transducer. An optical grating with sub-wavelength distance between fixed and moving grating fingers effectively changes the effective refractive index upon external excitation of the proofmass. The system houses an integrated VCSEL optical source on one side of the grating and a set of balanced photodetectors on the other side of the grating. A noise floor of 17 ng/ $\sqrt{\text{Hz}}$ was measured. Fourquette et al. [12, p. 266] from Michigan Aerospace created an optical MEMS-based accelerometer based on Whispering Gallery modes, which are morphology-dependent optical resonance shifts in small dielectric spheres. Accelerations as low as 10 ng/ $\sqrt{\text{Hz}}$ could be measured. Milligan et al. from HP [13], [14] have developed a closed loop silicon accelerometer using a periodic capacitive readout scheme, which ensures a linear readout. A Noise floor of 10 ng/ $\sqrt{\text{Hz}}$ was observed. Pike et al. [15], [16] have developed an accelerometer with a for MEMS very large silicon proofmass of 250 mg. It uses very compliant silicon flexures, capacitive readout and an inductive feedback loop. The accelerometer has a noise floor of 2 ng/ $\sqrt{\text{Hz}}$.

The sensors in this work are discussed separately. First the fourth generation 'Big Mass' accelerometer is discussed, after which the vertical demo accelerometer will be discussed.

II. NIKHEF G4 SENSOR

This section describes the design, simulation, fabrication and characterization of the fourth generation ultra sensitive

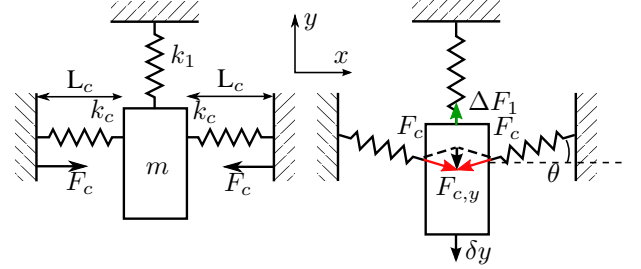


Fig. 1. A linearised representation of the principle of stiffness reduction through compression. Left: The mass m is at rest, the springs with stiffness k_c in the x -direction are compressed to a length L_c using compression force F_c . Right: the mass is displaced δy , inducing flexure rotation θ .

accelerometer developed in collaboration with the Nikhef institute. The sensor was not designed by the author, however, analysis and validation, part of the fabrication and the characterization results in this work are. The core of the Big Mass accelerometer consists of a proofmass system with precurved flexures. The flexures can be compressed using a set of thermal actuators and a nonreversible ratchet system. Compression of the flexures effectively reduces the stiffness of the system in the sensing direction, which is perpendicular to the compression direction. The sensitivity of the sensing direction well below the resonance is,

$$\frac{X}{A} = \frac{1}{\omega_0^2} = \frac{m}{k}, \quad (1)$$

in which X is the displacement of the proof mass, A is the applied acceleration, ω_0 is the resonance frequency, m is the proof mass and k is the stiffness of the mass-spring-system in the displacement direction. Equation (1) shows that if the stiffness decreases the sensitivity increases. A linearised model of the principle of reducing the stiffness in one direction by compression in another direction is shown in Figure 1. A proof mass m is connected to a spring in the y -direction of stiffness k_1 and 2 springs in the x -direction of stiffness k_c , which are compressed to length L_c using force F_c . The system is in equilibrium as the compression forces cancel out each other. Now the proof mass is displaced a small distance δy , so that the horizontal flexures are rotated a small angle θ . The force equilibrium in the vertical direction is described by,

$$F_{tot} = F_1 - F_{c,y}, \quad (2)$$

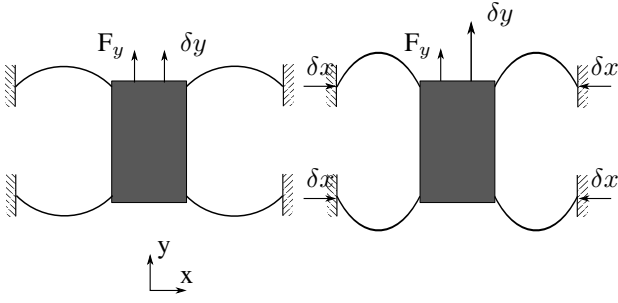


Fig. 2. A schematic representation of the big mass design shows the proof mass suspended by precurved flexures. Left: Uncompressed geometric anti springs, applying a force F_y in the sensitive y-direction results in a displacement δy of the proof mass. Right: As the flexures are compressed in the x-direction the displacement δy under the applied force F_y increases relative to the uncompressed state.

in which $F_1 = -k_1 \delta y$, and $F_{c,y} = 2F_c \sin \theta$. Now assuming small angle approximation and acknowledging that,

$$\tan \theta = \frac{\delta y}{L_c} \approx \theta, \quad (3)$$

the force balance becomes,

$$F_{tot} = - \left(k_1 - 2 \frac{F_c}{L_c} \right) \delta y. \quad (4)$$

The total stiffness k_{tot} in the vertical direction then is,

$$k_{tot} = \frac{F_{tot}}{\delta y} = k_1 - 2 \frac{F_c}{L_c}, \quad (5)$$

which shows that the total stiffness in the vertical direction is reduced by compressing the flexures in the horizontal direction. Figure 2 shows how the concept is applied to the accelerometer, the proof mass is suspended by a number of pre-curved flexures which can be compressed in the x-direction. Compressing the springs leads to a reduction of the stiffness in the y-direction, which is the sensing direction, and thus leads to an increase in sensitivity.

III. DESIGN BIG MASS ACCELEROMETER

The 4th generation Big Mass accelerometer consists of 3 slightly varying designs. A schematic representation of the G1.4 design is shown in Figure 3. The accelerometer has a symmetric design and the important structures are denoted as:

- 1) Proof mass
- 2) Flexures
- 3) Ratchet structure
- 4) Thermal actuators
- 5) Sense electrodes
- 6) Feedback electrodes
- 7) Alternative actuation electrodes

The proof mass of 30.5 mg is designed to be through-wafer, the height of the proof mass is 404 μm . The other structures are designed in the device layer, which has a thickness of 50 μm . Mass stops are incorporated into the design to prevent excess displacement which could result in fracturing of the device. The flexures suspend the proof mass. The flexures can be compressed by the thermal actuators and the ratchet structure ensures the flexures stay in the compressed state

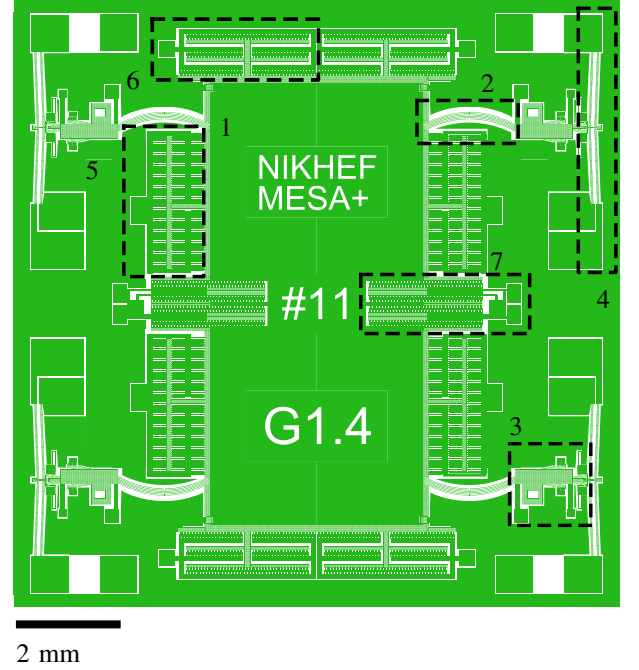


Fig. 3. Sensor design overview. Indicated in the picture: 1. Proof mass, 2. Proof mass Suspension Flexures, 3. Ratchet, 4. Thermal actuators, 5. Sense electrodes, 6. Feedback electrodes, 7. Alternative actuation electrodes .

without the need to power the device. The sense, feedback electrodes, and alternative actuation electrodes are electrostatic combdrives. The subsystems are explained deeper in the following subsections. The major design differences between the G1.4, G2.4 and G3.4 designs are the use of a more compliant suspension/straight guiding mechanism of the ratchet in the G2.4 design with respect to the G1.4 and G3.4 design, i.e. single beam flexure instead of triple parallel placed beam flexure. The G3.4 design uses nonlinear, but stronger, gap closing combdrive actuators as feedback actuator instead of the area changing combdrives used in the G1.4 and G2.4 design.

A. Compressed Spring Theory

A schematic representation of a precurved beam is shown in Figure 4. Denoted in Figure 4 are the length of the beam L , width w , height d , starting and end angles with respect to the horizontal axis respectively θ_0 and θ_L , initial radius R , arc length s running along the length of the beam and the angle of the beam with respect to the horizontal axis is $\theta(s)$. Concentrated forces, F_x and F_y , and moment, M_L , are applied to the tip. The material of the beam has Young's Modulus E and the cross section of the beam has a moment of inertia I . The internal forces are derived from the free body diagram as shown in Figure 5, in which $V(s)$ denotes the internal shear force along the beam arc length s , $M(s)$ is the beam internal moment, $N(s)$ is the internal normal force. The horizontal and vertical distance from the tip of the beam to the internal cross-section are respectively $x' = x_L - x(s)$ and $y' = y_L - y(s)$. The internal bending moment is shown in (6). The internal shear force is shown in (7).

$$M(s) = M_L + F_y x'(s) - F_x y'(s) \quad (6)$$

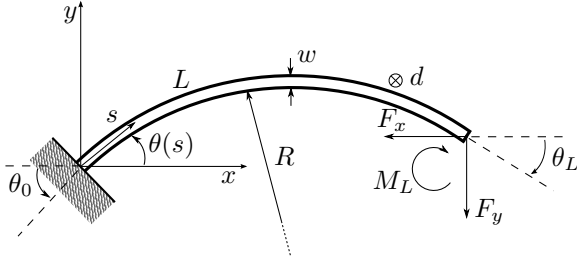


Fig. 4. Schematic representation of curved beam subjected to concentrated tip forces and moment.

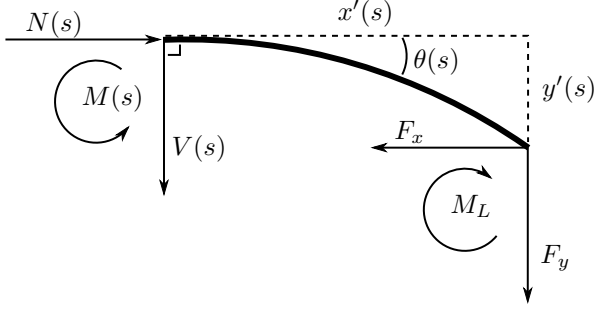


Fig. 5. Free body diagram of curved beam subjected to concentrated tip forces and moment.

$$V(s) = F_x \sin(\theta(s)) - F_y \cos(\theta(s)) \quad (7)$$

Standard beam theory, as shown in (8), describes the relation between the change in beam angle, $\delta\theta(s) = \theta(s) - \theta_i(s)$, and internal bending moment. The curvature is κ , the initial Young's modulus is E_1 , the initial second moment of area is I_1 , and $f(s)$ and $g(s)$ are functions describing the change in second moment of area and Young's modulus along the arc length. Differentiating (8) once more with respect to the arc length, assuming linear elastic material and uniform member cross-section $f(s) = g(s) = 1$, and substituting the internal shear force, a second order nonlinear ODE is found, (9).

$$\kappa = \frac{1}{R} = \frac{d\delta\theta(s)}{ds} = \frac{M(s)}{E_1 I_1 f(s) g(s)} \quad (8)$$

$$EI \frac{d^2(\theta(s) - \theta_i(s))}{ds^2} = F_x \sin(\theta(s)) - F_y \cos(\theta(s)) \quad (9)$$

The boundary conditions for the second order nonlinear ODE are the flexure's base and tip angle, as shown in (10). The tip angle rotation is fixed to represent a clamped-clamped situation. Furthermore for a constant initial radius the second derivative of the initial angle with respect to the arc length is zero.

$$\begin{aligned} \theta(0) &= \theta_0 \\ \theta(L) &= \theta_L \\ \frac{d^2\theta_i}{ds^2} &= 0 \end{aligned} \quad (10)$$

The second moment of area for a uniform rectangular cross section is [17],

$$I = \frac{dw^3}{12} \quad (11)$$

The design parameters of the flexures used in the Big Mass accelerometer are shown in table III.

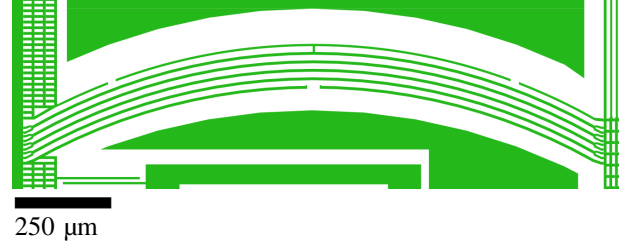


Fig. 6. Big mass accelerometer flexure design. The left end of the flexure is attached to the proofmass, the right end of the flexure is attached to the compression structure. Outer beams are satellite beams incorporated for the fabrication process.

TABLE III
DESIGN PARAMETERS BIG MASS ACCELEROMETER FLEXURES

Structure	Property	Parameter	Value
Flexures	Length	L	1732 μm
	Radius	R	1732 μm
	Width	w	8.66 μm
	Thickness	d	50 μm
	Base angle	θ_0	0.5 rad
	Tip angle	θ_L	-0.5 rad
	Initial stiffness	k_y	1 N/m
	Nr of flexures	n_s	16

B. Dynamic Model

The quasi-static 2 dimensional description of the dynamic behaviour of the tip is

$$\begin{pmatrix} \delta x(L) \\ \delta y(L) \end{pmatrix} = \begin{pmatrix} c_{xx} & c_{xy} \\ c_{xy} & c_{yy} \end{pmatrix} \begin{pmatrix} \delta F_x \\ \delta F_y \end{pmatrix} \quad (12)$$

in which $\delta x(L)$ and $\delta y(L)$ are the tip displacements, δF_x and δF_y are the applied forces and c_{ij} describes the compliance of the beam. The stiffness matrix can be found by inverting the compliance matrix. Adding a proof mass and suspending it into a viscous medium leads to a mass-spring damper system, for which the equations of motion are

$$m \frac{d^2 \delta y}{dt^2} + \gamma \frac{d \delta y}{dt} + n_s k_{yy} \delta y = f_{ext} \quad (13)$$

where the mass is described by m , the damping coefficient γ and the stiffness k_{yy} , the external forces are denoted by f_{ext} . The main direction of interest is the sensing direction, i.e. the y direction. Assuming a quasi static state, (13) simplifies to,

$$m \frac{d^2 \delta y}{dt^2} = -k_{yy} \delta y. \quad (14)$$

The resonant frequency $\omega_{0,y}$ of this system then is,

$$\omega_{0,y} = \sqrt{\frac{k_{yy}}{m}}. \quad (15)$$

The quasi-static sensitivity of a mass-spring system in terms of the displacement as a result of an applied acceleration is described by,

$$\frac{Y}{A} = \frac{1}{\omega_{0,y}^2} \quad (16)$$

TABLE IV
DESIGN PARAMETER SPECIFICATION G1.4

Structure	Property	Parameter	Value
Proof mass	Dimensions	L_m	8000 μm
		w_m	4000 μm
		h_m	404 μm
	Mass	m	30.5 mg
System (no compression)	Analytical	f_0	120 Hz
	Stiffness total	k_y	16 N m ⁻¹
	Rejection	k_x/k_y	60
		k_z/k_y	22

Which shows the compromise between bandwidth and sensitivity, an increase in sensitivity imposes a decrease in bandwidth. Using Laplace's transform on (13) and substituting the resonant frequency and quality factor $Q = \frac{\omega_0 m}{\gamma}$, the mechanical transfer function of the system from the externally applied force to displacement is obtained.

$$H(s) = \frac{Y(s)}{F(s)} = \frac{1}{s^2 + \frac{\omega_0}{Q}s + \omega_0^2} \quad (17)$$

The quality factor is a function of the resonant frequency, the mass and the damping coefficient. A high quality factor indicates an underdamped system. The response of a second order system is proportional below the natural frequency, and has a 40dB/da rolloff above the natural frequency.

The performance of the device on the lower limit will depend on its self-noise. The main source of noise without the electrical systems is the thermo-mechanical noise, also called Brownian noise, which originates from the random vibration of atoms in and around the system [18]. The noise equivalent acceleration of the mechanical system as a result of Brownian motion is,

$$a_b = \frac{1}{g} \sqrt{\frac{4k_B T \omega_0}{mQ}} [g/\sqrt{Hz}], \quad (18)$$

which is described by the Boltzmann constant k_B , the temperature T , the mass m and the Q-factor of the system Q . To obtain a low self-noise the resonance frequency must be as low as possible and the mass and Q-factor of the system should be as large as possible. In practice a high Q-factor can be obtained by reducing the viscous damping, i.e. by applying the proper vacuum conditions. Table IV shows the system design parameters regarding the mass-spring system.

C. Capacitive Sensing and Actuation

Readout is done using capacitive sensing. Big Mass devices utilize gap closing parallel plate comb drives for sensing, as shown in Figure 7. The capacitance C_{sense} of the sensing comb drives is,

$$C_{sense} = \epsilon_0 \frac{wd}{g_{sense} - \delta y} N_{sense} \quad (19)$$

in which ϵ_0 is the vacuum permittivity, d is the device layer height, w is the finger width, g_{sense} is the gap between rotor and stator fingers and N_{sense} is the number

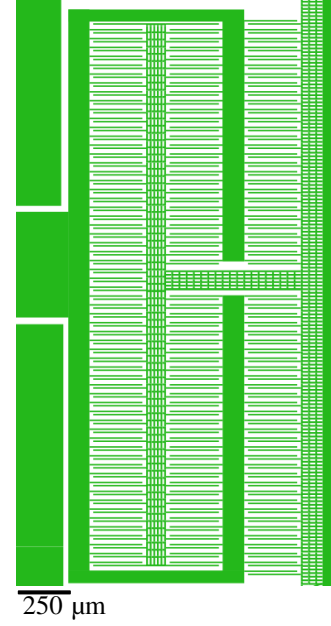


Fig. 7. Sensing combdrives design used in the Big Mass devices. Right side is fixed to proof mass.

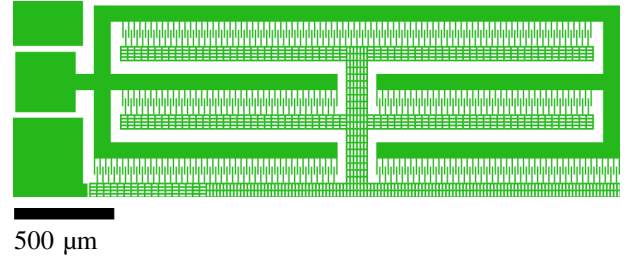


Fig. 8. Feedback actuator design G1.4 devices.

of rotor/stator pairs. Then sensing combs are designed in pairs so the capacitive readout can be done differentially. Actuation of the accelerometer is done by electrostatic forces. Electrostatic combdrives enable the actuation/compensation of the mass spring system. Two different sets of combdrives are incorporated in the design. First there are the combdrives at the top and bottom of the design, which are to be used for inplane feedback in closed loop operation. Second are the alternative actuation combdrives which can be used instead of the feedback combdrives. The G1.4 and G2.4 devices use area changing combdrives. Neglecting fringing effects and assuming capacitive contribution from tip to be comparatively small to the capacitance of the side of the fingers, the resultant force F_{elec} generated by N_{act} stator rotor finger pairs applying a potential difference V is,

$$F_{elec} = \epsilon_0 \frac{d}{g_{act}} N_{act} V^2 \quad (20)$$

where g_{act} is the gap between actuator combdrive fingers.

D. Pre-tensioning System

The nonreversible pre-tensioning system is realized using a novel ratchet system combined with a (double) thermal

TABLE V
DESIGN PARAMETER SPECIFICATION SENSING/ACTUATOR COMBDRIVES

Structure	Property	Parameter	Value
Sense electrodes	Finger length		250 μm
	Overlap		230 μm
	Gap size	g_{sense}	8 μm
	Pair count	N_{sense}	728
Feedback actuator	Type		G1.4, G2.4 G3.4
	Finger length		80 μm 250 μm
	Overlap		40 μm 235 μm
	Gap size	g_{act}	7 μm 8 μm
	Pair count	N_{act}	992 200
Alternative actuator	Finger length		80 μm
	Overlap		40 μm
	Gap size	g_{act}	7 μm
	Pair count	N_{act}	620

TABLE VI
DESIGN PARAMETER SPECIFICATION G1.4 COMPRESSION SYSTEM

Structure	Property	Parameter	Value
Thermal Actuator	Stroke	Δx_{TA}	15 μm
	Max load	$F_{x,TA}$	5600 μN
Compression (Ratchet)	First step		15 μm
	Thereafter		5 μm
	Max compression	Δx	35 μm

actuator. The thermal actuators, shown in Figure 10, are current driven. The silicon beams of the thermal actuator heat up under the flow of current through the structure, causing an expansion of the material. The center of the actuator pushes the ratchet structure under actuation, because the straight parts of the actuator meet up under an angle in the center. The stroke of the thermal actuator is designed to be at least 15 μm , providing a theoretical maximum load of 5600 μN . The thermal actuator moves to its original position while cooling down. The thermal actuator is integrated twice for redundancy. The limited stroke of the thermal actuator is overcome by the ratchet system, extending the total compression stroke of the system to 35+ μm . The layout of the ratchet system is shown in Figure 9. Under actuation the teeth at the end of the inclined compliant beams slide over and lock behind their counter-teeth. The ratchet system is doubly executed to obtain step increments of 5 μm . When the thermal actuator cools down another set of teeth locks into place to enable further compression at the next stroke of the actuator. The ratchet structure is straight-guided using a combination of folded and straight flexures. Table VI shows the design parameters for the compression system.

E. Release Design

The samples are released from the wafer using a dicing free release process as described in [19]. Release circles are incorporated into the design to guide the releasing process. The device layer is slowly underetched during a vapor-HF release etch, and the release circles are the last structures to release, ensuring a slow and gentle release. The mass stops (Figure 11)

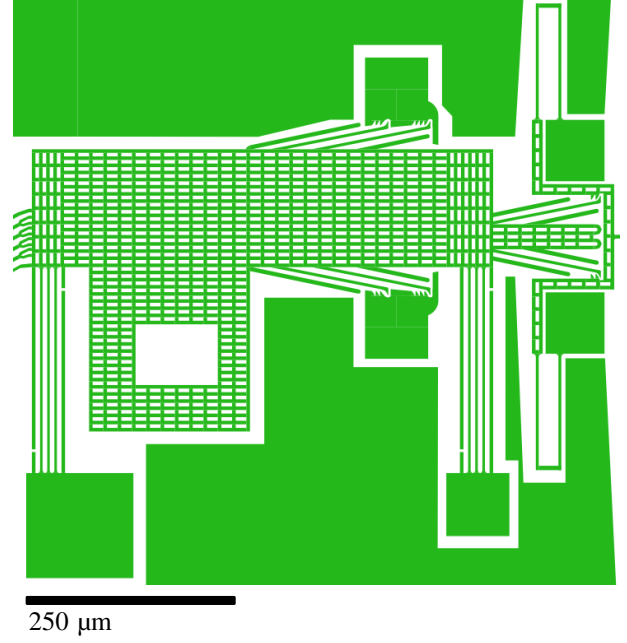


Fig. 9. Design of ratchet system enabling the compression of the proof mass suspension flexures.

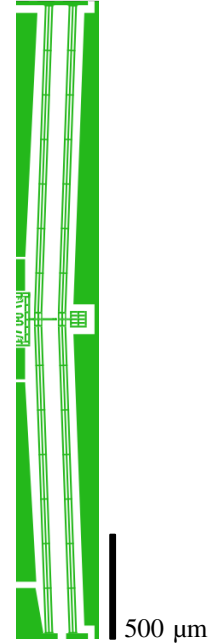


Fig. 10. Big mass thermal actuator design. The left end of the thermal actuator is attached to the ratchet system. The bottom and top of the thermal actuator are anchored through bondpads.

have release circles for the proof mass with a 15 μm diameter, while the outer edge of the device has release circles with a 20 μm diameter, i.e. the mass is suspended before the device is fully released.

IV. SIMULATION BIG MASS ACCELEROMETER

Several models were made to simulate the behaviour of the compression on the stiffness of the flexure. The dynamics of the system are investigated and a modal analysis is performed.

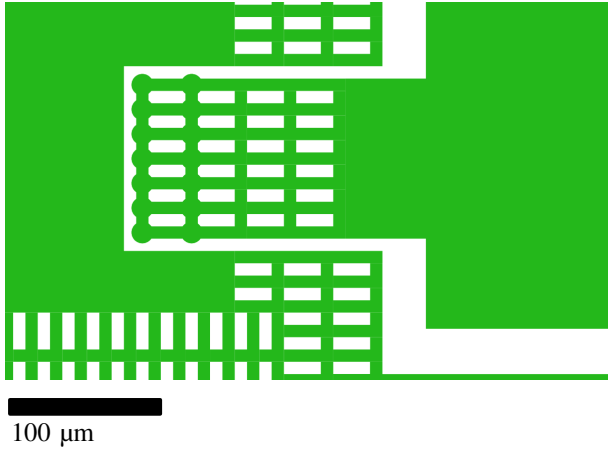


Fig. 11. Big mass accelerometer mass stop. Limits the in plane motion as well as the out of plane motion in the upward direction, also shows release circles guiding the release process.

A. Compressed Spring

First the stiffness behaviour of the flexures is investigated. It is generally very hard to solve nonlinear 2nd order ODE's like (9) analytically, therefore it was solved numerically using Matlab. Matlab's *bvp5c* boundary value problem solver was used, which is based upon the three-stage Runge-Kutta Lobatto Iiia formula [20]. Equation (9) is rewritten into a system of first order equations as the *bvp5c* solver requires, which is shown in (IV-A). The used code may be found in Appendix A.

$$\theta' = f(\theta) \quad (21)$$

$$\theta = \begin{pmatrix} \theta(s) \\ \theta'(s) \end{pmatrix} \quad (22)$$

$$\theta' = \begin{pmatrix} \theta'(s) \\ \theta''(s) \end{pmatrix} = \begin{pmatrix} \theta'(s) \\ \frac{1}{EI} F_x \sin(\theta(s)) - F_y \cos(\theta(s)) \end{pmatrix} \quad (23)$$

The numerical results were verified using Finite Element Modeling (FEM) in Comsol Multiphysics software and are in close agreement with each other. The flexure parameters used for modelling are shown in Table VII. For the 2 dimensional model of the flexure a plain stress situation is assumed. The geometry is meshed using quad elements. Tip displacements are applied instead of concentrated tip forces, because of the non-linear character of the compliance of the flexure and the stability of the FEM analysis in the Comsol software. The stiffness of the flexure is derived from the tip displacement and the reaction forces at the fixed base. The force F_x needed to compress the flexure a distance δx is shown in Figure 12. Above 1500 μN the analytical model becomes unstable. The change in inplane stiffness, k_y , perpendicular to the compression direction as a function of compression is shown in Figure 13. The numerical model predicts the stiffness of interest, k_y to become 'negative' at a compression of 35 μm . The stiffness reduction at a compression of 30 μm is predicted to be 9 fold. The out of plane stiffness is only marginally affected by compression of the flexure according to the 3D FEM model. The cross axis and out of plane rejection ratios

TABLE VII
FLEXURE PARAMETERS USED IN MODELING

Parameter	Value
Flexure length L	1732 [μm]
Flexure radius R	1732 [μm]
Base angle θ_0	0.5 [rad]
Tip angle θ_L	-0.5 [rad]
Flexure width w	8.66 [μm]
Flexure thickness d	50 [μm]
Young's modulus E	160 [GPa]
Moment of inertia $I = \frac{1}{12}dw^3$	2.71×10^{-21} [m^4]

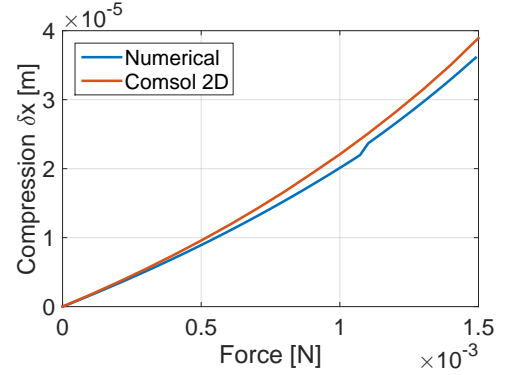


Fig. 12. Simulated force required for compression of the flexure. The force is applied in the compression direction.

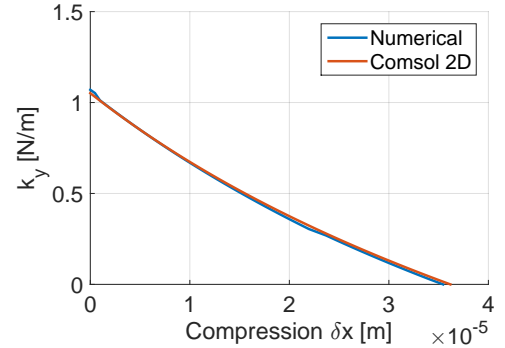


Fig. 13. Simulated change in vertical stiffness as function of compression.

are shown in Figure 15. The yield strength of monocrystalline silicon is up to 7000 MPa [21], but stress concentration factors of up to 33 around sharp corners have been seen [22]. Generally it is assumed safe to regard an upper stress limit of 300 MPa. The maximum stress found in the flexure at a compression of 35 μm from the FEM and numerical model is around 400 MPa, as shown in Figure 14, and occurs at the tips of the flexure. Filleting the attachment points of the flexure helps distributing the stress to safer values.

B. Dynamic Simulation

The flexure mechanics enable the prediction of the dynamics of the system. Using the stiffness and the known mass of the proof mass the change in resonance frequency of the system

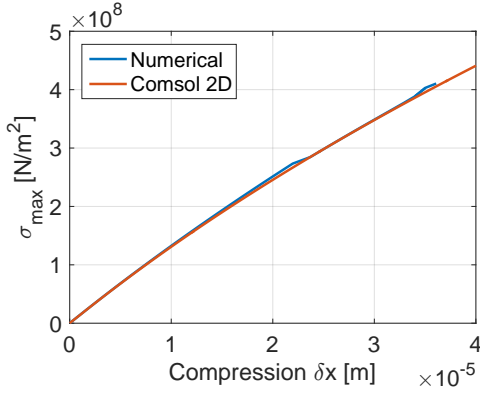


Fig. 14. Simulated maximum stress in flexure as function of compression.

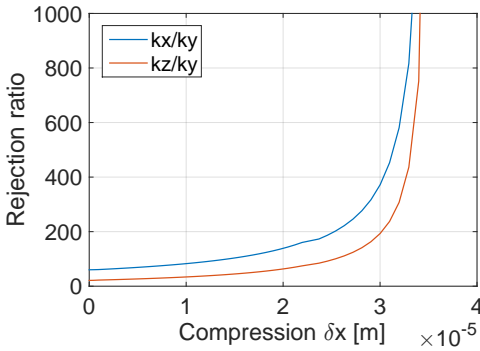
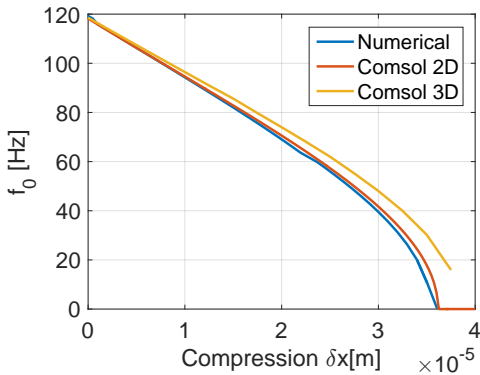
Fig. 15. Inplane and out of plane stiffness rejection ratios. Ratios go to infinity at 35 μm compression as stiffness k_y goes to zero in numerical model.

Fig. 16. Simulated change in resonance frequency versus flexure compression for several models.

can be calculated, which is shown in Figure 16. The numerical and 2D FEM solution are more compliant than the 3D FEM solution. The expected sag of the proof mass due to its own weight is $0.82 \mu\text{m}$. A modal analysis is performed on the full mass and 16 springs to find the modes of the system and their behaviour as the flexures are compressed. The first six modes without compression are shown in table VIII. Figure 17 shows the change in frequency for the modes as the flexures are compressed. The translational and rotational mode in and about the x -axis together with the translational mode in the y -axis change significantly as function of compression of the

TABLE VIII
SYSTEM MODES, NO COMPRESSION

Axis	DoF	Frequency
y	translation	118 Hz
z	translation	557 Hz
x	rotation	836 Hz
x	translation	868 Hz
z	rotation	1146 Hz
y	rotation	1371 Hz

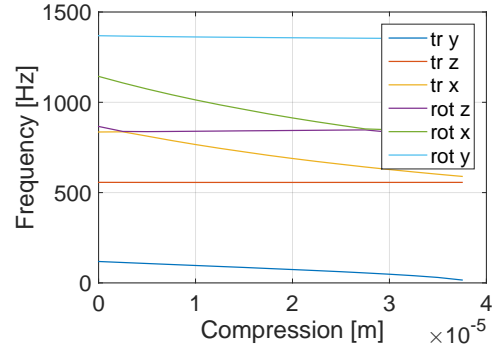


Fig. 17. Simulated change of frequency of several modes of the big mass accelerometer as function of compression.

flexures, while the translational and rotational z -axis mode and rotational y -axis mode change marginally.

V. FABRICATION BIG MASS ACCELEROMETER

The big mass accelerometer is fabricated using silicon-on-insulator (SOI)-wafer. The spring structures, actuators and read-out electrodes are processed in the device layer, while the mass includes the Buried Oxide (BOX) layer and part of the handle layer. A detailed process flow may be found in Appendix C. The fabrication of the big mass accelerometer is a three mask process. The substrate used is a P++-type SOI-wafer with an (100) orientation. The device layer has a thickness of $50 \mu\text{m}$. The buried oxide (BOX) layer has a thickness of $4 \mu\text{m}$. The handle layer has a thickness of $400 \mu\text{m}$. The process flow is shown in Figure 18.

A. Anisotropic KOH Etch

First a wet thermal oxidation step is done to create an oxide layer for patterning. The required oxide mask is created on the handle layer through photolithography using Olin907-17 photoresist, developing and then performing a deep reactive ion etching (DRIE) step. The wafer is now etched from the backside using a wet KOH etch step to create the recessed back of the proof-mass.

B. Device and Handle layer Etching

Another wet thermal oxidation step is performed to create a new oxide layer. The oxide layer on the handle layer is patterned using lithography to create an oxide mask. A DRIE

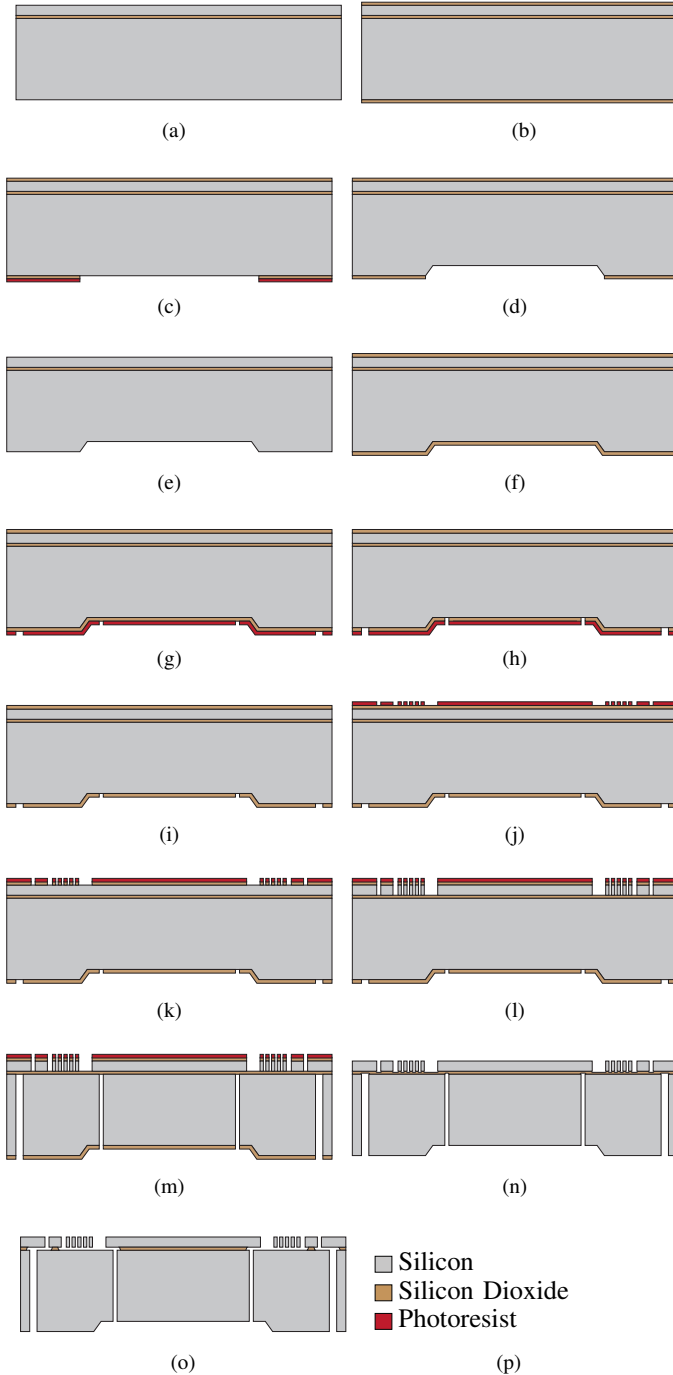


Fig. 18. Fabrication process: (a) SOI wafer, (b) oxidation, (c) lithography on handle layer, (d) KOH etch on handle layer, (e) oxide stripping, (f) oxidation, (g) photolithography on handle layer, (h) DRIE etch on handle layer, (i) resist strip, (j) photolithography on device layer, (k) oxide patterning, (l) DRIE etch on device layer, (m) DRIE etch on handle layer, (n) Resist and oxide strip, (o) HF vapor device release, (p) materials.

etching step is done to provide the etch mask for the cut-out of the proof-mass and to create the release grooves for the device. Then the oxide on the device layer is patterned using lithography and another DRIE etching step to obtain the etch mask for the flexures, actuators and readout electrodes. Another DRIE step up to the BOX layer creates the device layer features. A final DRIE step from the handle layer up to

the BOX layer creates the mass cut-out and release grooves.

C. Release Etch

Any residue fluor carbon from the DRIE etching is removed using O_2 plasma etching. A dicing free release method is chosen as the devices are very sensitive and prone to breakage as a result of impact and shock. The devices are released following the method as described in [19]. A vapor-HF etch at $37^\circ C$ for 45 min releases the devices on a wafer scale.

D. Results

The underetching of the devices in the vapor-HF etch step was checked by removing a release test structure with adhesive tape. After 45 min of vapor-HF the width of residue silicon dioxide of a $20\ \mu m$ diameter release circle was measured to be around $1.8\ \mu m$. Tapering of the flexures and combdrive electrodes was inspected after DRIE etching using scanning electron microscopy (SEM), the results are shown in Figure 19. Inspection through a microscope showed silicon spikes in some of the devices, as shown in Figure 20. These spikes most probably originate from the DRIE etching process. Several SEM images of the completed devices are shown in Figure 21. A photograph of the released devices is shown in Figure 22.

E. Final Assembly

After inspection the samples are mounted in 81 pins carriers using double sided conductive tape. The mounted samples are wirebonded and a microscope glass is hot glued on top of the carrier to seal and protect the devices. The final assembly is shown in Figure 23.

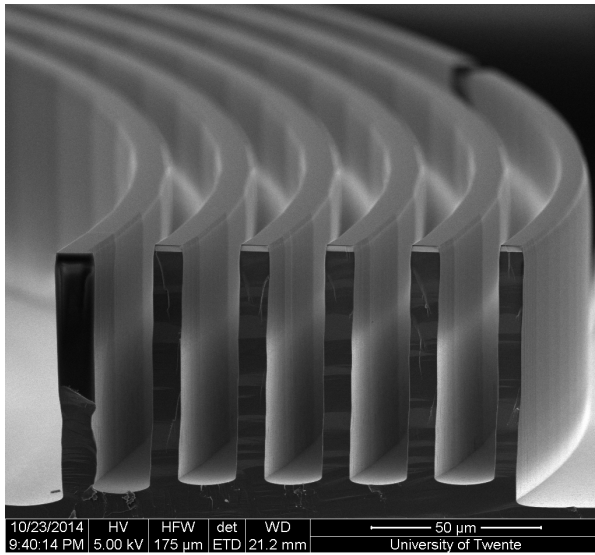
VI. CHARACTERIZATION BIG MASS ACCELEROMETER

The big mass accelerometer characterization focuses mostly on its in plane and out of plane mechanical properties. Electrical internal resistances of the accelerometer are also characterized.

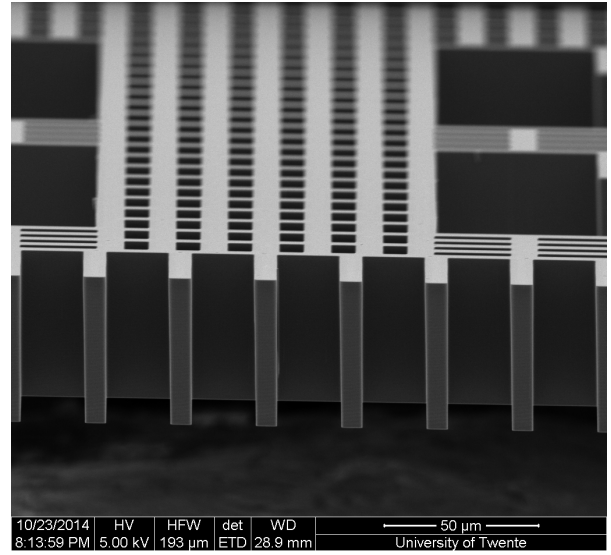
A. Setup

The carrier containing the sample is placed in a zif-socket inside a RFI box to minimize external electromagnetic interference. In-plane mechanical characterization is done using a Polytec MSA400 planar motion analyzer. In plane excitation of the proof mass is done using the electrostatic feedback combdrives of the big mass accelerometer. The handle layer and proof mass are grounded to prevent stiction as a result of static potentials. Then a potential is applied to the combdrive stator for actuation. A frequency sweep with a fixed amplitude and offset is applied.

Out of plane mechanical characterization is done using a Polytec MSA400 laser doppler vibrometer with a OFV5000 controller and an OFV552 fiber vibrometer. Static out of plane displacement are measured using white light interferometry on a Polytec MSA400. Dynamic characterization is done by vertical excitation of the sample with a piezoelectric actuator.



(a)



(b)

Fig. 19. Fabrication Results: (a) Bended flexure tapering inspection on dummy wafer, (b) Etch result of feedback actuator rotor electrodes, box side up

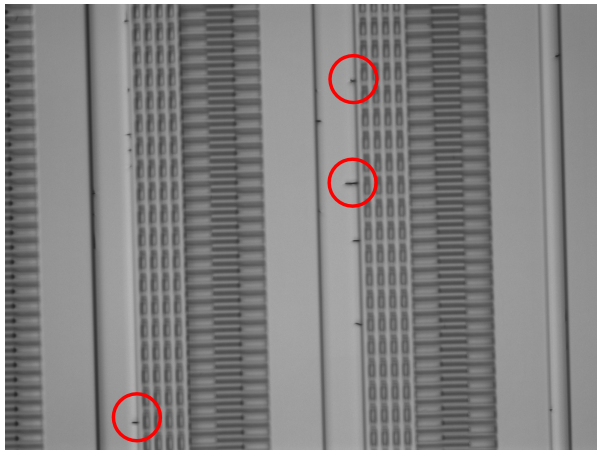


Fig. 20. Microscope image showing spikes which originate most probably from DRIE process.

The piezoelectric actuator has a resonance frequency of 1000 Hz. The actuator frequency is swept with fixed amplitude.

Ohmic resistances are measured using a Keithley digital multimeter and using 4-point probing where possible.

B. Mechanical Characterization

The static out of plane stiffness can be calculated from the vertical displacement of the mass. The sag at no compression was measured to be $1.75 \pm 0.25 \mu\text{m}$ across devices, together with a mass of 30.5 mg the out of plane stiffness would be $175 \pm 25 \text{ N m}^{-1}$ and the out of plane resonance frequency is expected to be $376 \pm 25 \text{ Hz}$.

A typical in plane frequency response curve for the big mass accelerometer is shown in Figure 24. The frequency response data is fitted against a second order transfer function model with 2 poles as shown in (17). A fit estimation of 95.9 % to the data was obtained. For the specific device the resonance

frequency is around 102 Hz with a Q-factor of 4 without compression. Other devices showed uncompressed resonance frequencies around 105 Hz with Q-factors up to 6.

A out of plane frequency response curve of a device is shown in Figure 25. The mode at 374 Hz is the internal resonance from the vibrometer. Peaks are found at 483, 620, 812, and 995 Hz. A 9-point measurement grid was used to visualize the found modes, not every mode visualization gave a clear image of which modes belong to the modes found in the modal FEM model. The FEM models stiffness was adjusted for the found out of plane stiffness. The 812 Hz mode found is the x-axis rotational mode. The spurious mode around 620 Hz is a combined in plane/out of plane diagonal swing mode, which was not found by the FEM analysis. Increasing the excitation voltage the first resonance mode (translational in z-axis) is found at 384 Hz for this specific device. Another device had its translational z-axis mode at 400 Hz. The 483 and 995 Hz modes could be from the setup used, i.e. resonances from the mounting of the sample, the modes of the mounting were not measured due to time constraints.

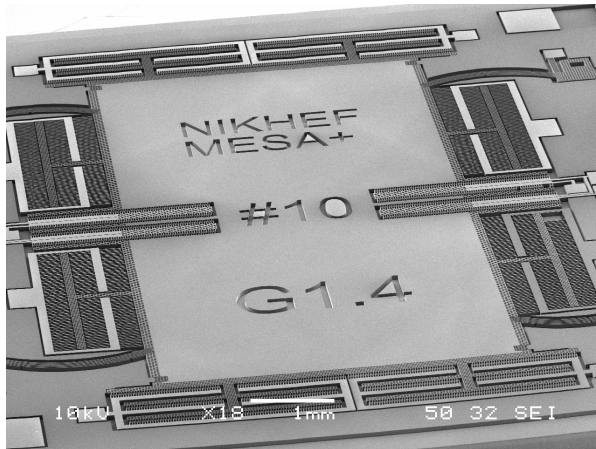
C. Electrical Characterization

The ohmic resistance of the thermal actuators at room temperature is measured to be $240 \pm 5 \Omega$. The maximum voltage applied to the thermal actuators before burning them is 26 V. The electrical resistance across the proof mass anchors was measured to be $329 \pm 1 \Omega$. The substrate resistance was measured to be $5.5 \pm 0.5 \Omega$. Some devices have an unexpected finite resistance from the alternative actuators to the substrate in the order of a few ten's of k Ω . This was not observed for the sensing or feedback electrodes.

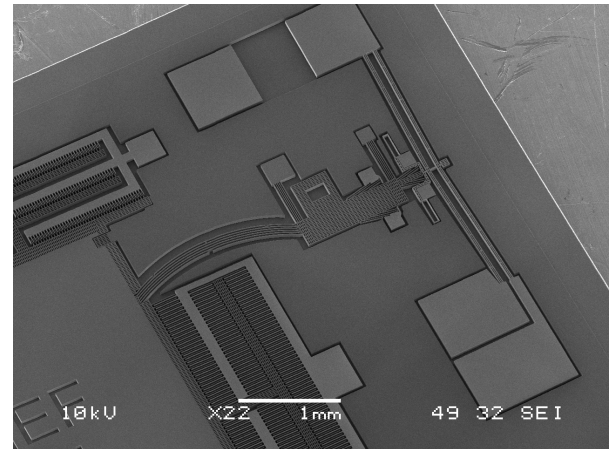
VII. DISCUSSION BIG MASS ACCELEROMETER

A. Satellite Beams

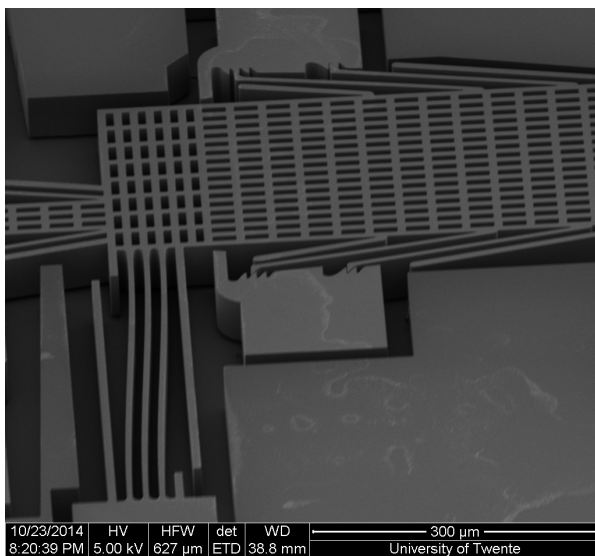
Compression to full state shows that the flexures are (almost) touching the satellite beams used for fabrication, shown



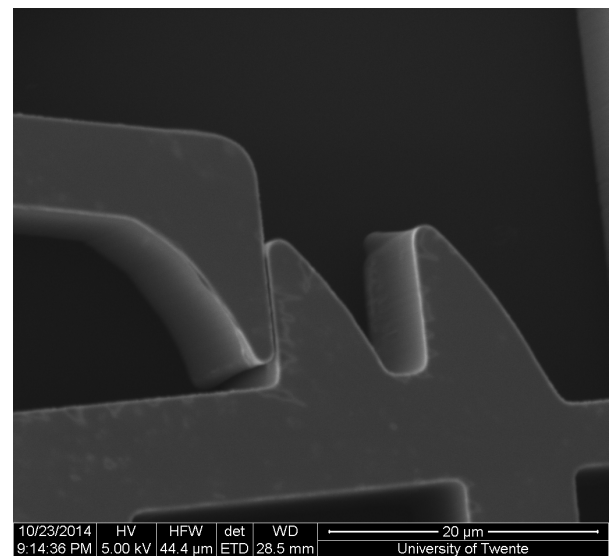
(a)



(b)



(c)



(d)

Fig. 21. Fabrication Results: (a) Device overview, (b) Thermal actuator, ratchet and flexures, (c) Ratchet in compressed state, (d) Closeup of ratchet teeth in compressed state

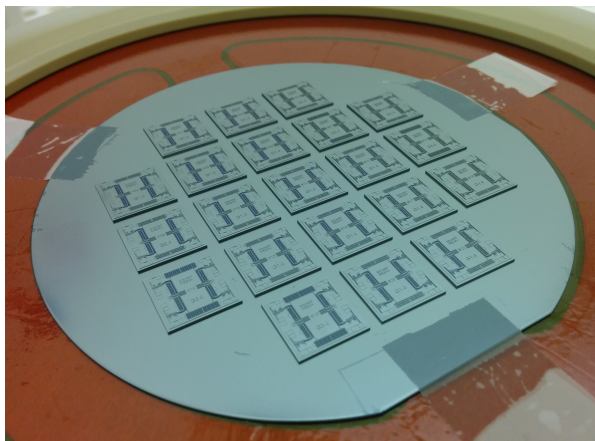


Fig. 22. Photograph showing the released devices after vapor-HF etching step.

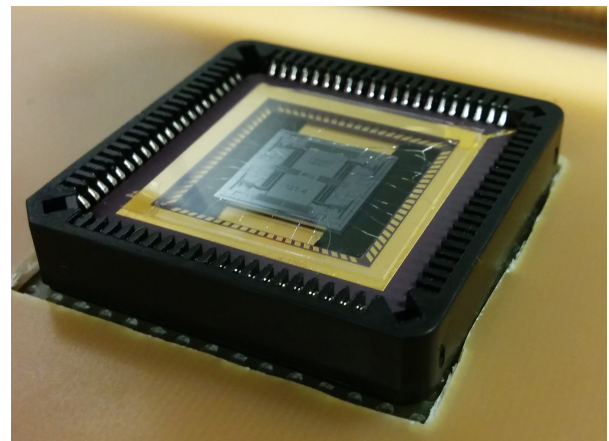


Fig. 23. Final assembly of the device, sealed carrier containing bondwired device is placed in zif-socket in this picture.

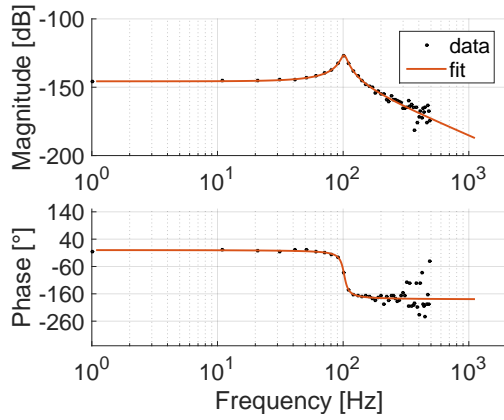


Fig. 24. In plane frequency response curve for big mass accelerometer, no compression, fitted with second order transfer function. 0 dB = 1 m.

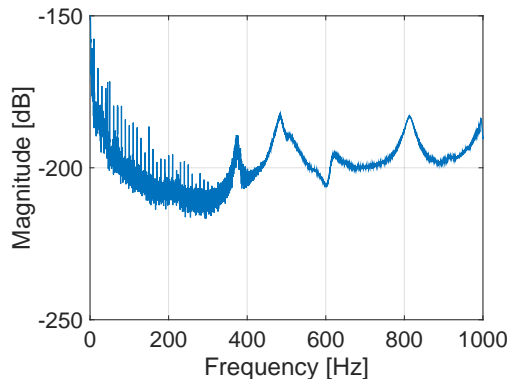


Fig. 25. Out of plane frequency response curve for big mass accelerometer. 0 dB = 1 m.

in Figure 26. This makes it hard to use the full compression range.

B. System Stiffness

The sag of the proof mass is considerably larger than expected from FEM simulations, i.e. 187.5 % larger, which indicates the system's out of plane stiffness is considerably lower than expected. This is confirmed by the out of plane resonant frequency of the system. The most probable cause is either a lower Young's modulus of the silicon or spring dimension variation due to the fabrication process. Measuring the out of plane resonant frequency was tricky as the internal resonance of the vibrometer interfered with the measurements. Increasing the excitation of the piezoelectric actuator to increase the response and overcome the internal resonance frequency led to stiction of some of the devices.

C. Stiction

One serious issue found during the characterization is a lack of robustness. A lot of the devices experienced stiction during the handling phases of the characterization. In most of the cases the feedback combdrives at the edges of the mass got stuck to the handle layer. One of the causes is the extreme sensitivity of the system. The final seismometer must be sufficiently robust to survive the handling from

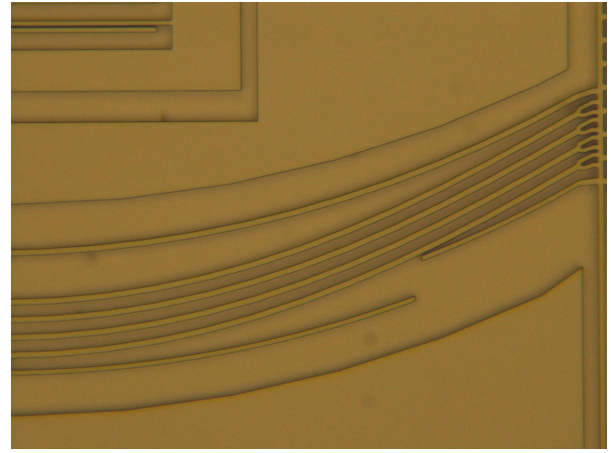


Fig. 26. Big mass accelerometer flexures in fully compressed state, satellite beams are nearly touching the outer flexure.

fabrication, assembly, transport and installation on site. Means to improve the robustness can be to reduce the mass, increase the stiffness, reduce the complexity of the system i.e. reduce the number of fingers in the combdrives or remove some of the combdrives entirely. Combdrives could be removed by introducing multiplexing of the sensing and feedback circuits. Reducing the number of combdrives/fingers will possibly also improve fabrication yield.

D. Eigenfrequencies Under Compression

Because of the stiction problems no clear mechanical characterization of the eigenfrequencies as function of compression could be done, other than the resonance frequencies with no compression.

E. Alternative Actuator Shortcut

The finite resistance measured from the tilt actuator to the handle layer requires further investigation. Observation through a microscope showed the presence of possible silicon spikes, usually found after DRIE etching. Further investigation could show whether the spikes have an influence on the short-cutting between actuator and handle layer.

VIII. CONCLUSIONS AND FUTURE WORK BIG MASS ACCELEROMETER

A fourth generation accelerometer was designed, fabricated and characterized. The ratchet system works very good, the stroke and force of the thermal actuators are sufficiently large. The stiffness of the measured devices was lower than expected by numerical and FEM models. Future work could include a redesign to obtain a more robust design. A more robust design could be achieved by decreasing the mass, increasing the flexure stiffnesses, decrease the number of combdrives and teeth. The satellite beam design should be adjusted to be able to achieve full compression state without touching the flexures. Mechanical characterization with the laser vibrometer can be expanded by measuring the resonant frequencies under various compressed states of the system. The system quality factor for

various compressions could be measured under various vacuum conditions. A vacuum setup with a piezoelectric actuator has been realized and is available for future measurements.

IX. VERTICAL SENSOR

As discussed in the introduction the Big Mass Accelerometer is unsuitable for use in the vertical direction. To achieve an operational sensor for a vertical orientation the flexures of the mass-spring system are rotated slightly upwards, see Figure 27. The angle of rotation of the flexures has to be determined such that at the required/predetermined compression the mass returns to the equilibrium position between the mass stops as a result of the gravitational acceleration of the mass when the sensor is placed vertically. This way the gravitational acceleration offset of 1 g is compensated. The focus in the vertical design is not to achieve extreme sensitivity, but to show the feasibility of a vertical implementation of a similar design.

X. DESIGN VERTICAL ACCELEROMETER

The overall vertical sensor design layout, as shown in Figure 28, shows a lot of similarities with the big mass accelerometer design. The features denoted in Figure 28 are,

- 1) Proof mass
- 2) Flexures
- 3) Ratchet structure
- 4) Thermal actuators
- 5) Sense electrodes
- 6) Feedback electrodes

The design parameters used for the vertical accelerometer are depicted in Table IX.

A. Mass Lifting by Compression

For the vertical accelerometer the flexure is rotated an angle ϕ . The vertical displacement of the tip $\delta y(L)$ only due to the rotation of the flexure is $\delta y(L) = x(L) \sin(\phi)$. The rotation of the flexures an angle ϕ is mathematically the same as rotating the applied concentrated tip forces changing (9) into,

$$EI \frac{d^2(\theta(s) - \theta_i(s))}{ds^2} = F_x \sin(\theta(s) + \phi) - F_y \cos(\theta(s) + \phi) \quad (24)$$

The vertical displacement of the tip due to compression is nonlinear, as shown in Figure 29.

B. Dynamic Model

The dynamic model is similar as described for the big mass accelerometer in section III-B.

C. Capacitive Sensing and Actuation

Sensing is done by measuring the change in capacitance of gap closing combdrives. The combdrive design is similar to the big mass accelerometer design, as described in section III-C, the main design difference is the finger pair count as the design space is more limited. Actuation is realized through lateral area changing combdrives which have the same dimensions

TABLE IX
DESIGN PARAMETER SPECIFICATION VERTICAL ACCELEROMETER

Structure	Property	Parameter	Value
Proof mass	Dimensions	L_m	2800 μm
		w_m	2780 μm
		h_m	25 μm
	Filling factor		71%
	Mass	m	0.32 mg
Flexures	Length	L	1000 μm
	Radius	R	1000 μm
	Thickness	w	5 μm
	Device layer height	d	25 μm
	Base angle	θ_0	0.5 rad
	Tip angle	θ_L	0.5 rad
	Flexure rotation angle	ϕ	0.102°
	Compression	Δx	18 μm
	Nr of flexures	n_s	4
Compression (Ratchet)	First step		17 μm
	Thereafter		1 μm
Thermal Actuator	Stroke at max load	Δx_{TA}	19 μm
	Max load	$F_{x,TA}$	400 μN
Sense electrodes	Finger length		250 μm
	Overlap		230 μm
	Gap size	g_{sense}	8 μm
	Pair count	N_{sense}	92
Feedback actuator	Finger length		80 μm
	Overlap		40 μm
	Gap size	g_{act}	7 μm
	Pair count	N_{act}	288
System	Analytical	f_0	390 Hz
	Stiffness total	k_y	2 N m ⁻¹
	Rejection	k_x/k_y	55
		k_z/k_y	23

as the big mass combdrives, again the main design difference is the fewer finger pair count. The designed stiffness of the vertical accelerometer is a factor 8 smaller than the big mass accelerometer, therefore the actuation can be less powerful.

D. Pre-tensioning and Lifting System

The pre-tensioning system is mostly similar to the one used in the Big Mass accelerometer as described in section III-D. The thermal actuator is smaller compared to the Big Mass design, as the design space for the vertical accelerometer demo was limited. The theoretical stroke of the thermal actuator is 19 μm and the maximum theoretical delivered force is 400 μN . The ratchet system has a more compliant straight guiding. The ratchet system is implemented in threefold to acquire 1 μm compression steps ranging from 16 to 18 μm per ratchet system, which is also shown in Figure 39. In practice this means the compression can be accurately controlled using 0.25 μm steps (average over four ratchet systems), enabling the compensation of possible deviation of flexure stiffness due to imminent fabrication process parameter variation.

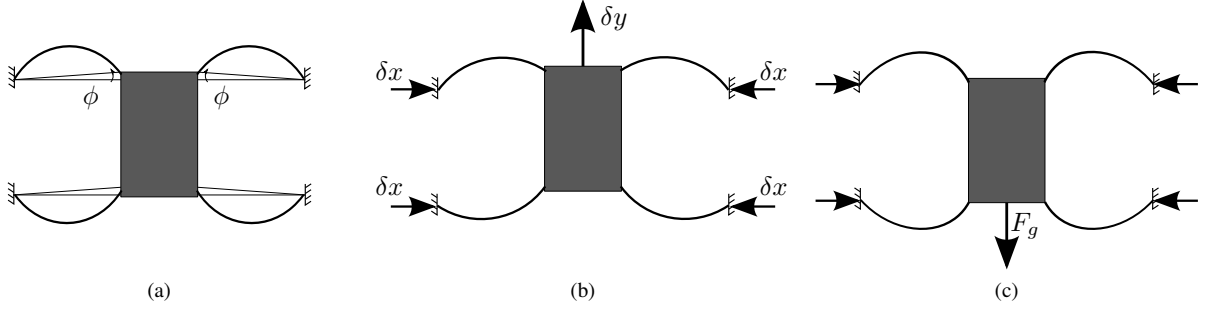


Fig. 27. Schematic illustration of the flexure rotation principle in the vertical accelerometer design. (a) The precurved flexures are rotated upwards by an angle ϕ . (b) The flexures are compressed in the horizontal plane causing the mass to move upwards. (c) The system is placed vertically and the proofmass lowers back into its equilibrium position, because of the gravitational acceleration.

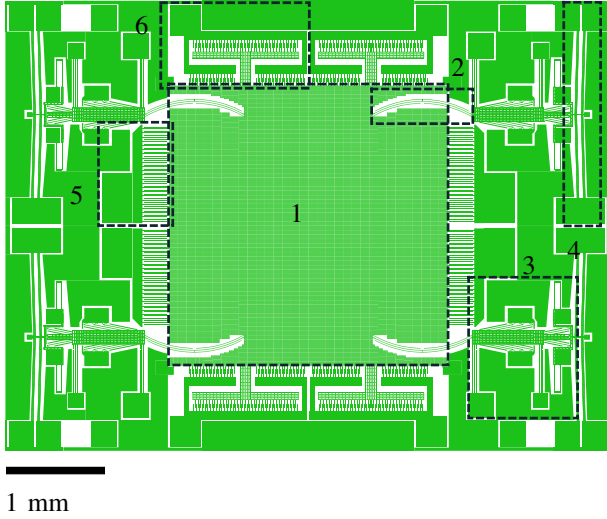


Fig. 28. Sensor design overview. Indicated in the picture: 1. Proof mass, 2. Proof mass Suspension Flexures, 3. Ratchet, 4. Thermal actuators, 5. Sense electrodes, 7. Feedback electrodes.

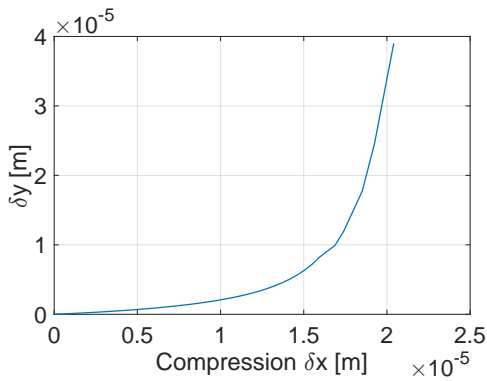


Fig. 29. Nonlinear change in vertical tip displacement as function of compression at a flexure rotation angle of 0.102° .

XI. SIMULATION VERTICAL ACCELEROMETER

The models used for simulation of the system characteristics are similar to the ones used for the big mass accelerometer as described in section IV, except for the used dimensions, and with the extension of the rotation of the flexures. The

TABLE X
FLEXURE PARAMETERS USED FOR MODELING OF VERTICAL ACCELEROMETER

Parameter	Value
Flexure length L	1000 [μm]
Flexure radius R	1000 [μm]
Base angle θ_0	0.5 [rad]
Tip angle θ_L	0.5 [rad]
Flexure width w	5 [μm]
Flexure thickness d	25 [μm]
Nr of elements N	1000
Young's modulus E	160 [GPa]
Moment of inertia $I = \frac{1}{12}dw^3$	2.60×10^{-22} [m ⁴]

numerical results were verified using Finite Element Modeling (FEM) in Comsol. The flexure parameters used for modeling are shown in Table X.

A. Compressed Spring

The force F_x needed to compress the flexure a distance δx is shown in Figure 30. The change in inplane stiffness, k_y , perpendicular to the compression direction as a function of compression is shown in Figure 31. The numerical model predicts the stiffness of interest, k_y to become 'negative' at a compression of 20.6 μm. The stiffness reduction at a compression of 18 μm is predicted to be 15 fold. The out of plane stiffness is only marginally affected by compression of the flexure according to the 3D FEM model. The in plane cross axis and out of plane rejection ratios are shown in Figure 33.

B. Spring Rotation

The required spring rotation angle is found by applying the designed compression of 18 μm, then applying a vertical force on the tip due to the gravitational acceleration of the mass and sweeping the flexure rotation angle. The resulting vertical tip deflection as a function of rotation angle is then fitted and the required flexure rotation angle at which the mass rests in its neutral position is extracted. For the designed mass of 0.32 mg and the flexure design parameters as described in table X, this leads to a required flexure rotation angle of 0.102° .

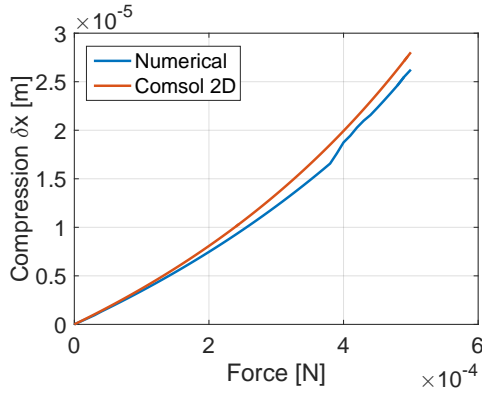


Fig. 30. Simulated force required for compression of the flexure. The force is applied in the compression direction.

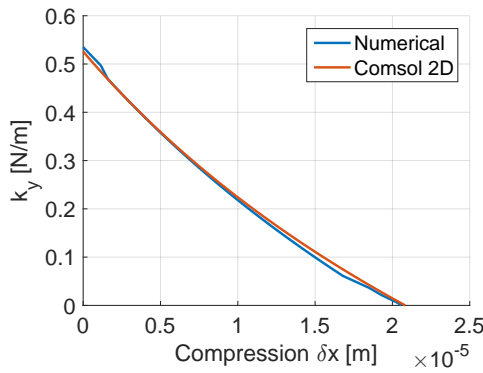


Fig. 31. Graph showing the change in vertical stiffness as function of compression for several models.

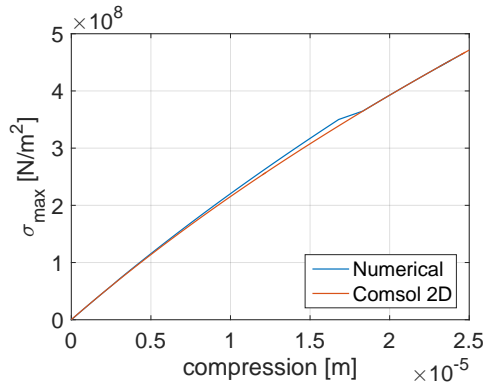


Fig. 32. Graph showing the stress as function of compression for several models.

C. Dynamic Simulation

The Eigenfrequency of the sensing direction as a function of flexure compression is shown in Figure 34. A modal analysis was performed using a 3D FEM model of the mass and springs, the resonant frequencies of 6 fundamental modes as function of compression are shown in Figure 35. The Eigenfrequencies of the fundamental modes at a compression of 18 μm are also shown in Table XI.

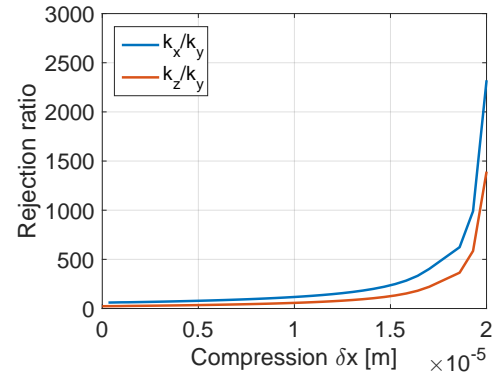


Fig. 33. Inplane and out of plane stiffness rejection ratios. Ratios go to infinity at 20.6 μm compression as stiffness k_y goes to zero in numerical model.

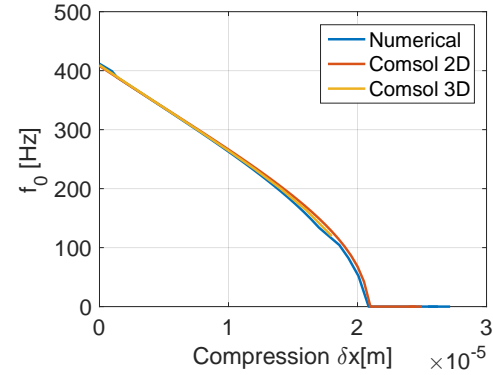


Fig. 34. Graph showing the change in vertical eigenfrequency as function of compression for several models.

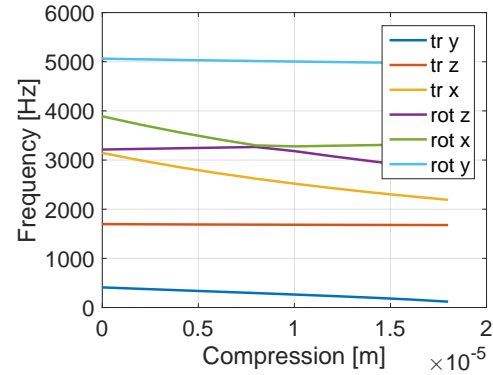


Fig. 35. Graph showing the change in vertical eigenfrequency as function of compression for several models.

TABLE XI
SYSTEM MODES, AT 18 μm COMPRESSION

Axis	DoF	Frequency
y	translation	120 Hz
z	translation	1677 Hz
x	translation	2192 Hz
z	rotation	2801 Hz
x	rotation	3328 Hz
y	rotation	4967 Hz

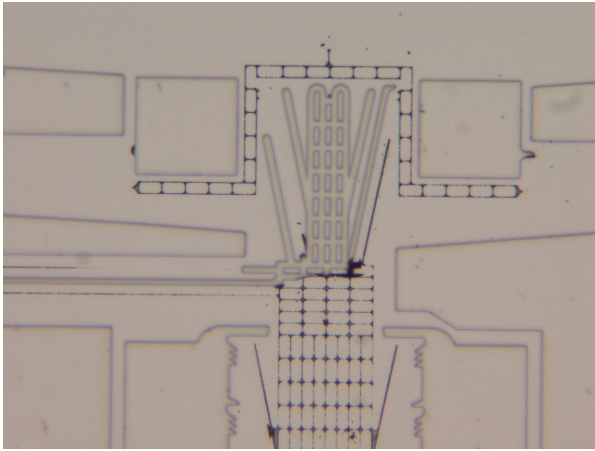


Fig. 36. Photograph showing leftover silicon oxide below ratchet structure after vapor-HF etching step.

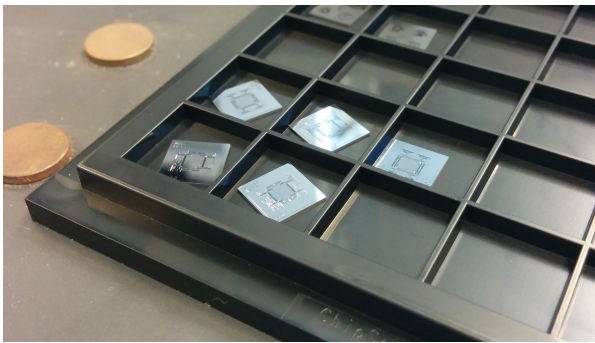


Fig. 37. Photograph showing vertical demo accelerometers after fabrication.

XII. FABRICATION VERTICAL ACCELEROMETER

The fabrication of the proof of concept vertical accelerometer comprises of a two-mask process. The substrate for the vertical accelerometer is a P++-type SOI-wafer with an (100) orientation. The device layer has a thickness of 25 μm . The BOX layer has a thickness of 2 μm , while the handle layer has a thickness of 380 μm . In contrary to the big mass accelerometer process there is no recessed mass, and thus no KOH etching step on the backside of the handle layer. The fabrication process further is identical to the big mass accelerometer process as described in section V.

A. Results

First fabrication results showed the HF-vapor etch duration was too short, as shown in Fig. 36, which shows the leftover silicon oxide below the ratchet structure. Devices after fabrication are shown in Figure 37. A bondwired vertical accelerometer is shown in Figure 38. A close up of the ratchet structure with a compression of 17 μm is shown in Figure 39.

B. Final Assembly

After microscope inspection the samples were fixed inside 81 pins carriers using double sided conductive adhesive tape. The samples were then wirebonded and a glass cover was placed over the device.

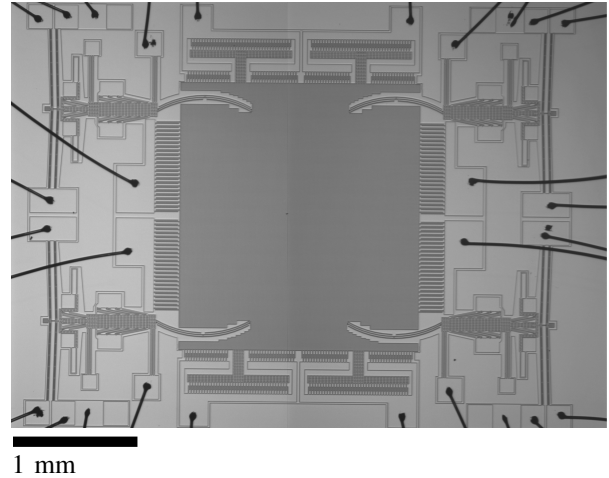


Fig. 38. Microscope picture of bondwired vertical accelerometer.

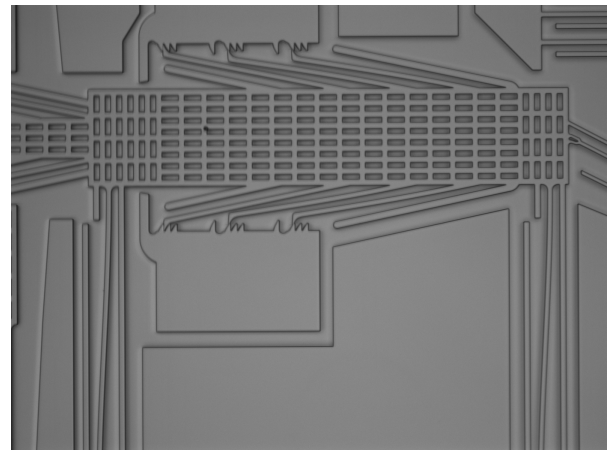


Fig. 39. Close up of one of the gearboxes of a vertical accelerometer. Compressed to 17 μm .

XIII. CHARACTERIZATION VERTICAL ACCELEROMETER

In this section an overview is given of the measurement results on the vertical demo accelerometer. The setup is discussed after which the mechanical characterization is reviewed.

A. Setup

At higher compressions the vertical accelerometers proof mass presses against its mass stops in the horizontal position. A setup has been realised to observe and measure the vertical demo accelerometer at higher compressions with the vibrometer. A schematic representation of the setup is shown in Fig. 40, the actual setup is shown in Figures 41,42. A mirror is placed at 45° on a micrometer screw scanning table, the rotation about the z- and y-axis can be adjusted to optimize focus. The sample is placed vertically inside a zif-socket on a xy-scanning table. The in plane motion of device is realised through electrostatic actuation with the feedback combdrives. The proof mass and handle layer are grounded while a signal is applied to the combdrive stator. The in plane motion is then measured by the planar motion analyzer of the vibrometer.

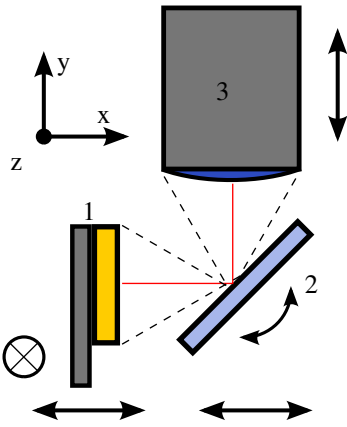


Fig. 40. Schematic representation of the setup used to view and measure the vertical accelerometer demo in its vertical state with the vibrometer. Denoted in the picture: 1. Vertically placed device, 2. Mirror at approximately 45°, 3. Vibrometer lens.

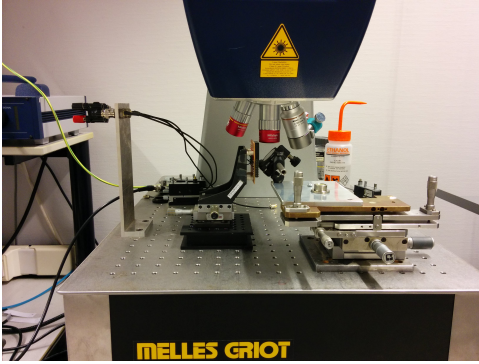


Fig. 41. Setup used to characterize vertical accelerometer.

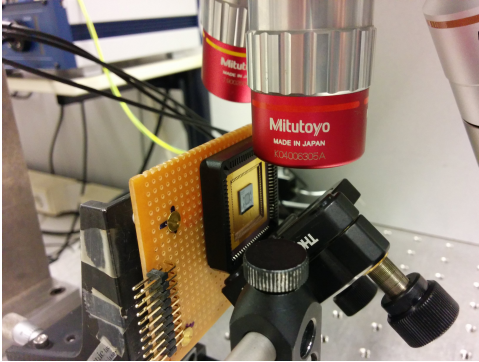


Fig. 42. Close up of setup used to characterize vertical accelerometer.

B. Mechanical Characterization

The thermal actuators were not strong enough to enable the first ratchet step. Compression had to be realized through careful manual manipulation using a micrometer accurate probe. In plane horizontal frequency versus compression is shown in Figure 44. The numerical model (24) is fitted to the data points. The fitted parameter is the product of the Young's modulus E and the moment of inertia I . The compression force F_x is adjusted to match the compression δx after a first fit of the product EI . Then the process is repeated to obtain

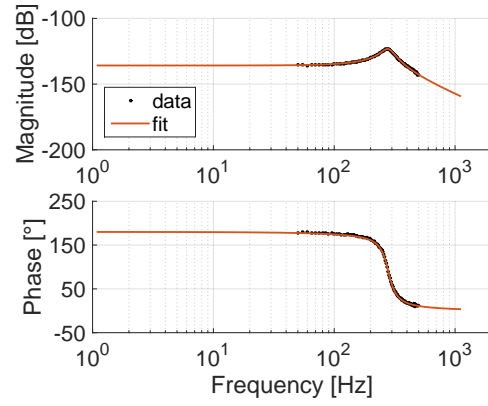


Fig. 43. Frequency response of vertical accelerometer with a compression of 8.5 μm .

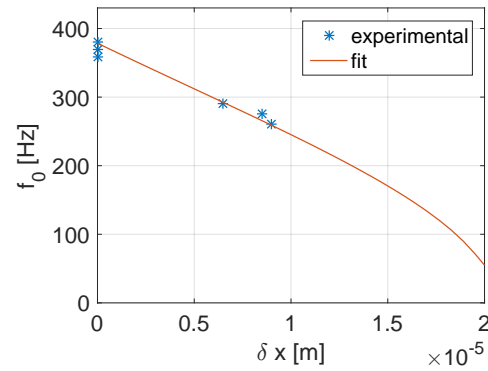


Fig. 44. Graph showing model fit on experimental data.

a optimal fit. This is necessary as the numerical model uses the compression force F_x as input instead of the compression δx . The design assumed a Young's modulus of 160 GPa and a moment of inertia of $2.6 \times 10^{-22} \text{ m}^4$ which leads to an EI of $4.17 \times 10^{-11} \text{ Nm}^2$. The fitted EI is $3.58 \times 10^{-11} \text{ Nm}^2$, which is 14.2 % smaller. A 2 fold stiffness reduction was observed at a compression of 9 μm , reducing the resonant frequency of the device from 370 to 260 Hz. A sample with a flexure rotation angle of 0.095° was compressed to 8.5 μm average compression and placed vertically. Figure 45 shows the proof mass between the mass stops. The vertical distance between the mass stop and the proof mass is measured $6.0 \pm 0.5 \mu\text{m}$, which means the vertical displacement of the proof mass relative to it neutral position is $-1.0 \pm 0.5 \mu\text{m}$. The numerical model predicts a vertical displacement of $-1.6 \mu\text{m}$. The image quality acquired in the vertical setup was quite low and did not suffice dynamic mechanical characterization of the sensor in the vertical stance through the planar motion analyzer. A dynamic characterization was performed but did not return a sufficient signal to noise ratio.

XIV. DISCUSSION VERTICAL ACCELEROMETER

A. Vertical Setup

The current vertical setup has too many degrees of freedom and makes it difficult to get a decent image quality for dynamic

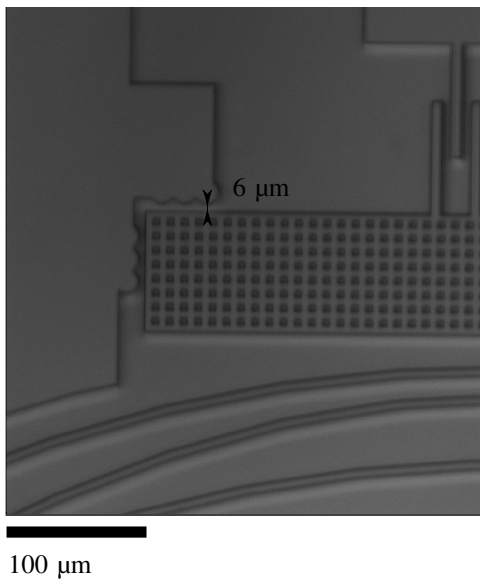


Fig. 45. Microscope image of vertically placed demo accelerometer with 8.5 μm compression, shown is the upper left mass stop and part of the flexures and proof mass. The proof mass is almost in its original position between the mass stops.

characterization through the planar motion analyzer. Static characterization is possible.

B. Thermal Actuators and Ratchet System

The stroke delivered by the thermal actuators was not large enough for the ratchet to reach the required first step of 17 μm , therefore the ratchet had to be controlled manually using probes with micrometer accurate precision. This was quite time consuming and sometimes led to breakage of part of the sensor. The most probable source for the failure of the thermal actuators is the increased bending stiffness of the ratchet system due to the addition an extra set of pawls for more precise stepping. Furthermore the spacing of the subsequent pawls meant the tooth of the pawl rests on top of the fixed tooth, all pawls have to bend at the same time while compressing. Less precise stepping could be considered in a next design iteration as such precise stepping is not really necessary.

C. Stiction

A lot of devices failed due to stiction issues occurring during the handling phases of the characterization. More sensitive handling and less handling steps could reduce the number of failed devices due to shock and stiction.

XV. CONCLUSIONS AND FUTURE WORK VERTICAL ACCELEROMETER

A vertical accelerometer demo was designed, fabricated and characterized. A setup was realized to characterize the devices in a vertical position under the vibrometer. Although the thermal actuator did not work sufficiently devices were characterized in a compressed state in the horizontal plane. The stiffness was reduced by a factor 2 at 9 μm compression

decreasing the first fundamental mode of the system from 370 to 260 Hz. A compressed device was placed vertically and the proof mass was observed to displace to a position close to the expected value. This shows that the approach of mechanical compensation of the gravitational offset is feasible. Future work could benefit from a vertical setup with a reduced number of DOF's. It would be beneficial to be able to control the angle under which the sample is placed to have some control over the gravitational force on the mass. Another device batch may enable the characterization under full compression. Future work may include a redesign with stronger thermal actuators, a decreased average step size of the ratchet system, an increase of the mass to increase the sensitivity or application of the rotated flexures to the big mass accelerometer design.

XVI. OVERALL CONCLUSIONS

A 4th generation MEMS accelerometer for Newtonian noise subtraction arrays was modelled, partly fabricated and mechanically characterized by the author. The compression system works very well. The sensor turned out to behave less stiff than expected by the models. A first demo vertical MEMS accelerometer was designed, modelled, fabricated and mechanically characterized. A vertical setup for characterization through the planar motion analyzer of the vibrometer has been realised and enables static measurements. For dynamic measurements the image quality is not yet sufficient, this is believed to be caused for the most part by the difficult alignment of vibrometer lense, mirror and device. The flexure rotation showed to be a feasible compensation mechanism for the gravitational offset of 1 g. The vertical accelerometer showed a 2-fold stiffness reduction under an average flexure compression of 9 μm .

ACKNOWLEDGMENT

The author would like to thank his wife Eva for her never ending support and motivation, and his kids Sterre, Mees and Valentijn for their inspiration. Remco Wiegerink, Robert Brookhuis, Remco 'Pino' Sanderink and Eric Hennes for their patience, support and fruitful discussions.

REFERENCES

- [1] N. van Bakel, "Silent sensors for stellar echo's and seismic surveys," June 2013.
- [2] T. Accadia, F. Acernese, M. Alshourbagy, P. Amico, F. Antonucci, S. Aoudia, N. Arnaud, C. Arnault, K. Arun, P. Astone *et al.*, "Virgo: a laser interferometer to detect gravitational waves," *Journal of Instrumentation*, vol. 7, no. 03, p. P03012, 2012.
- [3] F. Acernese, M. Agathos, K. Agatsuma, D. Aisa, N. Allemandou, A. Allocca, J. Amarni, P. Astone, G. Balestri, G. Ballardin *et al.*, "Advanced virgo: a second-generation interferometric gravitational wave detector," *Classical and Quantum Gravity*, vol. 32, no. 2, p. 024001, 2015.
- [4] J. Laine and D. Mogenot, "A high-sensitivity mems-based accelerometer," *The Leading Edge*, vol. 33, no. 11, pp. 1234–1242, 2014.
- [5] B. J. Merchant, "Mems applications in seismology," in *Seismic Instrumentation Technology Symp, NSF*, 2009.
- [6] Kinemetrics, "Episensor 2," Datasheet. [Online]. Available: <http://www.kinemetrics.com/uploads/PDFs/Episensor%202%20Datasheet.pdf>
- [7] Endevco, "Model 86," Datasheet. [Online]. Available: <https://www.endevco.com/86/>

- [8] C. Garcia, G. Onaran, B. Avenon, M. Christensen, Z. Liu, N. Hewa-kasakarage, and N. Hall, "Micro-seismometers via advanced meso-scale fabrication," Silicon Audio, Tech. Rep. [Online]. Available: <http://www.osti.gov/scitech/servlets/purl/1027453>
- [9] D. Carr, P. Baldwin, H. Milburn, and D. Robinson, "A laser interferometric miniature seismometer," in *Proceedings of the 2011 Monitoring Research Review: Ground-Based Nuclear Explosion Monitoring Technologies*, 2011.
- [10] T. Abramovich, I.A. and Zhu, "Next generation robust low-noise seismometer for nuclear monitoring," in *Proceedings of the 2009 Monitoring Research Review: Ground-Based Nuclear Explosion Monitoring Technologies*, Sep 2009. [Online]. Available: <http://www.osti.gov/scitech/servlets/purl/992203>
- [11] U. Krishnamoorthy, R. H. Olsson, G. R. Bogart, M. S. Baker, D. W. Carr, T. P. Swiler, and P. J. Clews, "In-plane mems-based nano-g accelerometer with sub-wavelength optical resonant sensor," *Sensors and Actuators A: Physical*, vol. 145-146, pp. 283-290, 2008. [Online]. Available: http://ac.els-cdn.com/S0924424708001672/1-s2.0-S0924424708001672-main.pdf?_tid=6b7ebc06-9bef-11e4-befb-00000aab0f6b&acdnat=1421241513_04cc651d39228fcd25744d8f9c8c8ae
- [12] D. Fourguette, V. Ötügen, L. Larocque, G. Ritter, J. Meeusen, and M. Kennedy, "Optical mems-based seismometer," in *Proceedings of the 2011 Monitoring Research Review: Ground-Based Nuclear Explosion Monitoring Technologies*, Sep 2011. [Online]. Available: <http://www.osti.gov/scitech/servlets/purl/1027453>
- [13] D. Milligan, B. Homeijer, and R. Walmsley, "An ultra-low noise mems accelerometer for seismic imaging," in *Sensors, 2011 IEEE*, Oct 2011, pp. 1281-1284.
- [14] B. Homeijer, D. Milligan, and C. Hutt, "A brief test of the hewlett-packard mems seismic accelerometer," pp. 20141047, 18 p., 2014. [Online]. Available: <http://dx.doi.org/10.3133/ofr20141047>
- [15] W. Pike, I. Standley, and S. Calcutt, "A silicon microseismometer for mars," in *Solid-State Sensors, Actuators and Microsystems (TRANSDUCERS EUROSENSORS XXVII), 2013 Transducers Eurosensors XXVII: The 17th International Conference on*, June 2013, pp. 622-625.
- [16] W. Pike, A. Delahunty, A. Mukherjee, G. Dou, H. Liu, S. Calcutt, and I. Standley, "A self-levelling nano-g silicon seismometer," in *SENSORS, 2014 IEEE*, Nov 2014, pp. 1599-1602.
- [17] R. Hibbeler, *Mechanics of Materials*. Pearson Prentice Hall, 2011. [Online]. Available: <https://books.google.nl/books?id=HikDQgAACAAJ>
- [18] T. Gabrielson, "Mechanical-thermal noise in micromachined acoustic and vibration sensors," *Electron Devices, IEEE Transactions on*, vol. 40, no. 5, pp. 903-909, May 1993.
- [19] I. Sari, I. Zeimpekis, and M. Kraft, "A full wafer dicing free dry release process for mems devices," *Procedia Engineering*, vol. 5, pp. 850-853, 2010.
- [20] S. G. Pinto, S. P. Rodríguez, and J. M. Torcal, "On the numerical solution of stiff ivps by lobatto iiia runge-kutta methods," *Journal of computational and applied mathematics*, vol. 82, no. 1, pp. 129-148, 1997.
- [21] K. E. Petersen, "Silicon as a mechanical material," *Proceedings of the IEEE*, vol. 70, no. 5, pp. 420-457, 1982.
- [22] K. Sooriakumar, W. Chan, T. S. Savage, and C. Fugate, "A comparative study of wet vs. dry isotropic etch to strengthen silicon micro-machined pressure sensor," in *Electrochem. Soc. Proc.*, vol. 27, 1995, pp. 259-265.
- [23] R. Brookhuis, "Big mass accelerometer - process document," Oktober 2015.

APPENDIX A MATLAB CODE

The following Matlab code was used to obtain the results from numerically solving the second order nonlinear differential equations describing the prestressed, precurved beam.

curvedbeambvp.m

```
function [theta] = curvedbeambvp(N,s,L,d,w,E,I,Fx,Fy,theta0,thetaL,dphi)

%Initial solution structure
solinit = bvpinit(linspace(0,L,2),@mat4init);
%ODE numerical solution
sol = bvp5c(@mat4ode,@mat4bc,solinit);
%Mesh grid, arc length
s = linspace(0,L,N);
%Extract angle as function of arc length s
theta = deval(sol,s);

%-----
%Rate equations
function dthetads = mat4ode(s,theta)
    dthetads = [ theta(2)
                1/(E*I)*(Fx*sin(theta(1) + dphi) -Fy*cos(theta(1) + dphi) )];

end

%Boundary conditions
function res = mat4bc(thetaa,thetab)
    res = [thetaa(1) - (theta0)
           thetab(1) - (thetaL)];

end

%Initial guess structure
function thetaint = mat4init(s,theta)
    thetaint = [(theta0)
                (thetaL)];

end
end
```

curvedbeamsolve.m

```
function [dx_num,dy_num,kx_num,ky_num,stress_max_num,Ustrain_num] = curvedbeamsolve
%Parametric curve with constant radius
close all
N = 1000; %Number of elements in beam
theta0 = 0.5; %beam base angle [rad]
thetaL = -0.5; %beam tip angle [rad]
dphideg = 0; %flexure rotation [deg]
dphi = dphideg*(pi/180); %flexure rotation [rad]
L = 1732e-6; %beam length [m]
R = L/(abs(theta0-thetaL)); %Curved beam initial radius [m]
si = linspace(0,L,N); %parameter initial arc length [m]
x0 = -R*sin((theta0)); %horizontal position beam base [m]
y0 = R*cos((theta0)); %vertical position beam base [m]
xL = -R*sin((thetaL)); %horizontal position beam tip [m]
yL = R*cos((thetaL)); %vertical position beam tip [m]
xi = R*sin(si/R -(theta0))-x0; %horizontal position along beam with origin in beam base [m]
yi = R*cos(si/R -(theta0))-y0; %vertical position along beam with origin in beam base [m]
thetai = theta0 - si/R; %initial angle along beam [rad]
dthetaidsi = -1/R; %derivative initial angle along beam [rad/m]
s = linspace(0,L,N); %arc length parameter [m]

%Plot initial curve
figure('Units','Pixels','Position',[100,100,1600,800])
subplot(3,3,1)
plot(xi,yi)
    %title('initial vs deformed flexure')
    xlabel('x [m]')
    ylabel('y [m]')
```

```

%initialize parameters for beam
rho_Si = 2330;           %Density Silicon [kg/m^3]
d = 50e-6;              %device layer height [m]
E = 160e9;              %Youngs modulus Silicon [Pa]
w = 8.66e-6;            %Spring width [m]
I = (1/12)*d*w^3;        %area moment of inertia [m^4]
%A = 1.38808875*10^(-6); %Surface quarter mass calculated by clewin [m^2] (Vertical accelerometer)
mass = 30.5e-6;          %Total mass [kg]
g = 9.81;               %Gravitational acceleration constant [m/s^2]
n_spring = 16;          %nr of springs

Fg = -mass*g/n_spring;   %Force due to gravity
Fx = -1400e-6;           %Compression force [N]
Fy = 0 ;                 %Acceleration force [N]

%Run bvp solver, obtain numerical solution

theta = curvedbeamvp(N,s,L,d,w,E,I,Fx,Fy,theta0,thetaL,dphi);

%Calculate x- and y-position of beam along arc length
x(1) = 0;
y(1) = 0;
for n = 2:numel(s)
    x(n) = L/length(s)*cos((theta(1,n)+theta(1,n-1))/2)+ x(n-1);
    y(n) = L/length(s)*sin((theta(1,n)+theta(1,n-1))/2)+ y(n-1);
end

%Plot beam shape
hold on
plot(x,y)
hold off
subplot(3,3,2)
plot(s,theta(1,:))
    %title('angle along arc length')
    xlabel('s [m]')
    ylabel('\theta [rad]')

%Calculate and plot delta angle along arc length
dtheta = theta(1,:) - thetai;
subplot(3,3,3)
plot(s,dtheta)
    %title('\Delta\theta(s)')
    xlabel('s [m]')
    ylabel('\Delta\theta [rad]')

%Calculate and plot delta x- and y-positions along arc length
dx_num = x-xi;
dy_num = y-yi;
dx_num(1)
dxtip = dx_num(end)
dy_num(1)
dytip = dy_num(end)

subplot(3,3,4)
plot(s,dx_num)
    %title('dx')
    xlabel('s [m]')
    ylabel('\Delta x [m]')

subplot(3,3,5)
plot(s,dy_num)
    %title('dy')
    xlabel('s [m]')
    ylabel('\Delta y [m]')

%Calculate and plot Moment along beam
M_s = E*I*(theta(2,:)-dthetaidsi);
subplot(3,3,6)
plot(s,M_s)
    %title('Moment along arc length')
    xlabel('s [m]')
    ylabel('M(s) [Nm]')
subplot(3,3,7)

%Calculate and plot maximum stress along beam

```

```

stress_max_num = 0.5*w*M_s/I;
plot(s, stress_max_num)
    title('\sigma_{max} along arc length')
    xlabel('s [m]')
    ylabel('\sigma_{max} [Nm^2]')

%% Run sweep over applied forces
% problem value sweep
FxVals = linspace(0, -1490e-6, 51); % Compression force
FyVals = linspace(0, 1e-6, 21); % Vertical displacement force values
[FxGrid, FyGrid] = meshgrid(FxVals, FyVals); % Grid of sweep values

% Reserve memory solution
xend = zeros(size(FxGrid));
yend = zeros(size(FxGrid));
M_s_max_num = zeros(size(FxGrid));
M_s = zeros(numel(FxVals), numel(FyVals), numel(s));
stress_max_num = zeros(size(FxGrid));
Ustrain_num = zeros(size(FxGrid));

%run curvedbeambvp, sweep over all value combinations
tic;
for jdx = 1:numel(FxVals)
    for idx = 1:numel(FyVals)
        theta = curvedbeambvp(N,s,L,d,w,E,I,FxGrid(idx,jdx),FyGrid(idx,jdx),theta0,thetaL,dphi);
        for n = 2:numel(s)
            x(n) = L/length(s)*cos((theta(1,n)+theta(1,n-1))/2)+ x(n-1); %Calculate x,y positions along beam
            y(n) = L/length(s)*sin((theta(1,n)+theta(1,n-1))/2)+ y(n-1); %Solution matrices of tip displacements
            xend(idx,jdx) = x(end);
            yend(idx,jdx) = y(end)+xend(idx,jdx)*sin(dphi);

            M_s_max_num(idx,jdx) = E*I*(max(theta(2,:))-dthetaidsi); %Calculate maximum Moment along beam
            M_s(idx,jdx,:) = E*I*(theta(2,:))-dthetaidsi; %Moment along arc length
            stress_max_num(idx,jdx) = 0.5*w*M_s_max_num(idx,jdx)/I; %Maximum stress along beam
        end
    end
end

tend = toc;
fprintf('Elapsed time is %4.3f seconds. \n', tend);

close all
dx_num = abs(xend - xend(1,1)); %Calculate compression
dy_num = yend - yend(1,1); %Calculate vertical displacement
kx_num = -FxGrid./dx_num; %Calculate horizontal stiffness
ky_num = FyGrid./dy_num; %Calculate vertical stiffness
w0 = sqrt(ky_num/((1/n_spring)*mass)); %Resonant frequency system
f0 = w0/(2*pi);

%%
% Stiffness ratios
kz = E*w*d^3/L^3; %Out of plane stiffness approximation
dz_sag = -(mass*g)/(n_spring*kz) %Out of plane sag
kzky = kz/ky_num(2,1); %Rejection ratio kz/ky
ky_ratio = bsxfun(@rdivide,ky_num,ky_num(:,1)); %Nominal stiffness change ky/ky0
kxky_ratio = bsxfun(@rdivide,kx_num,ky_num); %Rejection ratio kx/ky
kzky_ratio = kz./ky_num; %Rejection ratio kz/ky

%% Vertical accelerometer angle dphi determination
clear Fx Fy xend yend
dphi = linspace(0, 0.12*(pi/180),11);
Fx = -215e-6;
Fy = Fg;

tic;
for i = 1:numel(dphi)
    theta = curvedbeambvp(N,s,L,d,w,E,I,Fx,Fy,theta0,thetaL,dphi(i));
    for n = 2:numel(s)
        x(n) = L/length(s)*cos((theta(1,n)+theta(1,n-1))/2)+ x(n-1); %Calculate x,y positions along beam
        y(n) = L/length(s)*sin((theta(1,n)+theta(1,n-1))/2)+ y(n-1); %Solution matrices of tip displacements
        xend(i) = x(end);
        yend(i) = y(end)+xend(i)*sin(dphi(i));
    end
end
tend = toc;

```

```
fprintf('Elapsed time is %4.3f seconds. \n', tend);

%Fit dphi vs yend curve
[dy_tip_fit,gof] = fit(dphi',yend','poly1')
phi_dy_tipZero = fzero(dy_tip_fit, dphi(1))
phi_dy_tipZero_deg = phi_dy_tipZero * (180/pi)
dy_tip_verification = dy_tip_fit(phi_dy_tipZero)

%Fit structure, gof = goodness of fit
%Solve rotation angle phi for dy_tip_fit(phi) == 0, in [rad]
%In [deg]
%Verification of rotation angle
```

APPENDIX B MASKS LAYOUT

A. Overview

The process requires a total of 3 masks. One mask to create the recessed proof-mass in the handle layer, one mask for etching the structures in the device layer and a mask to create the cut-out of the proof mass and to create release grooves.

- 1 *KOH* Patterning of oxide on handle layer to create KOH etching mask for recessed mass



Fig. 46. Cross-sectional view after using mask *KOH*.

- 2 *HANDLE* Patterning of oxide on handle layer to create pattern for proof-mass cut-out and release grooves



Fig. 47. Cross-sectional view after using mask *HANDLE*.

- 3 *DEVICE* Patterning of oxide on device layer to create pattern for the spring, sensor and actuator structures

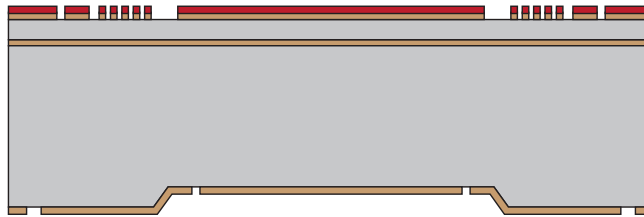


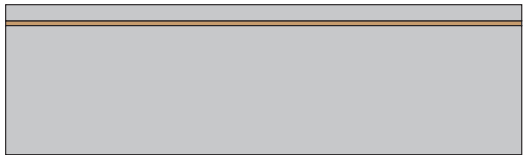
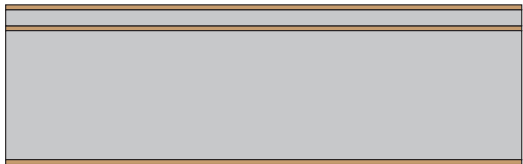
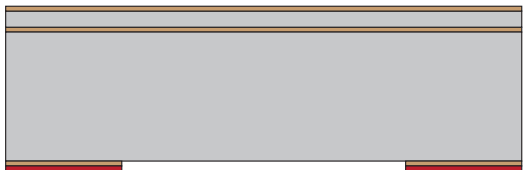
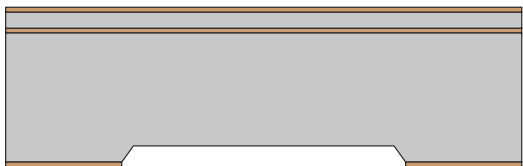
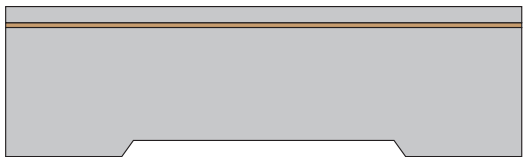
Fig. 48. Cross-sectional view after using mask *DEVICE*.

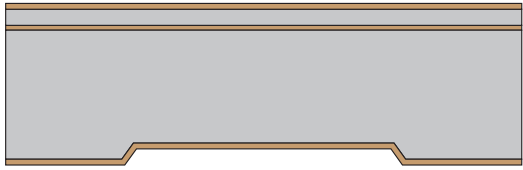



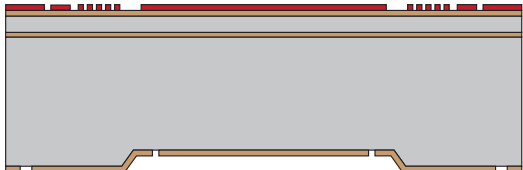
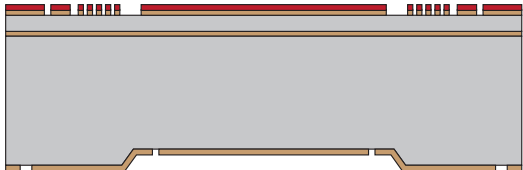
B. Summary

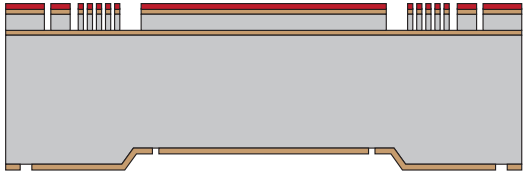
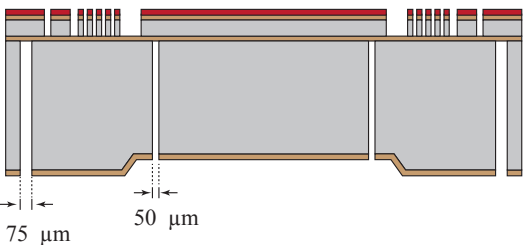
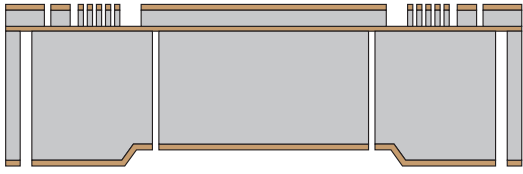
Mask	Description	Name	Layer	Inside white/black
1	Oxide etch to create KOH etching mask for recessed mass	<i>KOH</i>	1	Inside white
2	Oxide etch to create release pattern and proof-mass cut-out	<i>HANDLE</i>	2	Inside white
3	Oxide etch to create structures in device layer	<i>DEVICE</i>	3	Inside white

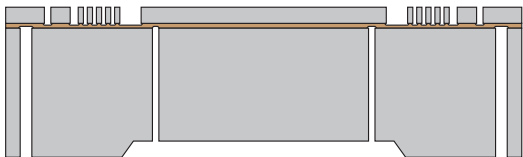


APPENDIX C

PROCESS OUTLINE

Step	Process	Cross-section after process
1	<ul style="list-style-type: none"> Substrate selection SOI 50-4-400 Orientation: $\langle 100 \rangle$ Highly doped, P++ 	
2	<ul style="list-style-type: none"> Wafer cleaning Wet Thermal Oxidation, 300 nm Temperature, 1000°C Time: 1:10 h Measurement of oxide layer thickness Remark: Oxide layer should be chosen thicker for next run. Damages due to KOH etching are observed at the device layer. 	
3	<ul style="list-style-type: none"> Coating handle layer with photoresist, Olin 907-17 Exposure, mask: KOH Etching of silicon dioxide in Adixen DE depth: 300 nm time: < 1 min. 	
4	<ul style="list-style-type: none"> Etching silicon of handle layer in KOH depth: 50 μm estimated time: ≈ 50 min. Remark: etching rate can vary, check with dummy wafers and inspect the depth with profilometer after etching. Total etching time used: 67 min (4 SOI wafers + 1 dummy) 	
5	<ul style="list-style-type: none"> RCA cleaning Oxide removal using 50% HF Pre-furnace cleaning 	

6	<ul style="list-style-type: none"> Wet Thermal Oxidation, $2\mu\text{m}$ Temperature, 1150°C Time: 12 h Measurement of oxide layer thickness 	
7	<ul style="list-style-type: none"> Spraycoating of photoresist Exposure, mask: <i>HANDLE</i> 	
8	<ul style="list-style-type: none"> Etching of silicon dioxide in Adixen DE depth: $2\mu\text{m}$ time: ≈ 5 min. 	
9	<ul style="list-style-type: none"> Cleaning of wafer, stripping resist 	
10	<ul style="list-style-type: none"> Coating device layer with photoresist, Olin 907-17 Exposure, mask: <i>DEVICE</i> Vacuum contact: check pressure should, be better than -0.8 bar. 	
11	<ul style="list-style-type: none"> Etching of silicon dioxide in Adixen DE depth: $2\mu\text{m}$ time: ≈ 5 min. 	

12	<ul style="list-style-type: none"> • DRIE Etching of silicon in Adixen SE, top side • Recipe: RB.HARS, see process document [23] for process details. • depth: 50 μm • time: ≈ 17 min. • Remark (1): all photoresist will be consumed during etching • Remark (2): due to highly directional etching recipe, spikes can occur especially in large open (exposed) areas. The SF6 etching time can be increased slightly (0.1 s) if too many spikes are observed. 	
13	<ul style="list-style-type: none"> • DRIE Etching of silicon in Adixen SE, bottom side • Recipe: Pulsed-C4F8-Topside, for process parameters see process document [23]. • depth: 400 μm • time: ≈ 36 min. • Remark (1): check if trenches at the edge of the wafer are also completely etched. Hold wafer against light to see if all trenches are transparent. • Remark (2): the trenches at the side are wider than the trenches in the middle to compensate for the difference in height. In case of a re-design of the mask, this difference in width should be increased (e.g. to 80 μm (trench) and 40 μm (mass)) 	
14	<ul style="list-style-type: none"> • Fluor carbon removal • O2 plasma cleaning, 800 Watt, 1 hour • Piranha cleaning, 30 min. 	

15	<ul style="list-style-type: none">• Etching of oxide in 50% HF• Time: ca. 2 min. until oxide at top and bottom side is removed	 A cross-sectional diagram of a semiconductor device. It shows a central rectangular region with a thin layer on top. On either side of this central region are two larger rectangular blocks. The top surface of the central region and the top surfaces of the side blocks are covered by a thin, uniform layer. The bottom surfaces of the side blocks are exposed.
16	<ul style="list-style-type: none">• Vapor-HF to release of proof-mass and devices• Time: 45 min.• Temperature: 37 °C• Use dummy structures in between the samples to check the etching result.	 A cross-sectional diagram of a semiconductor device, similar to the one in step 15. It shows a central rectangular region with a thin layer on top. On either side of this central region are two larger rectangular blocks. The top surface of the central region and the top surfaces of the side blocks are covered by a thin, uniform layer. The bottom surfaces of the side blocks are exposed.
17	<ul style="list-style-type: none">• Release samples by removing surrounding frame• Measurement/Inspection of samples	 A cross-sectional diagram of a semiconductor device, similar to the one in step 15. It shows a central rectangular region with a thin layer on top. On either side of this central region are two larger rectangular blocks. The top surface of the central region and the top surfaces of the side blocks are covered by a thin, uniform layer. The bottom surfaces of the side blocks are exposed.